Development of NIR-responsive Thin Film for Chemo-photothermal Therapy in the Treatment of Breast Cancer

M.Sc. Thesis

By
MILAN KHANDA



DEPARTMENT OF BIOSCIENCES AND BIOMEDICAL ENGINEERING

INDIAN INSTITUTE OF TECHNOLOGY INDORE

MAY, 2025

Development of NIR-responsive Thin Film for Chemo-photothermal Therapy in the Treatment of Breast Cancer

A THESIS

Submitted in partial fulfillment of the requirements for the award of the degree

of

Master of Science

by

MILAN KHANDA



DEPARTMENT OF BIOSCIENCES AND BIOMEDICAL ENGINEERING

INDIAN INSTITUTE OF TECHNOLOGY INDORE

MAY, 2025



INDIAN INSTITUTE OF TECHNOLOGY INDORE

CANDIDATE'S DECLARATION

I hereby certify that the work which is being presented in the thesis entitled "Development of NIR-responsive Thin Film for Chemo-photothermal Therapy in the Treatment of Breast Cancer" in the partial fulfillment of the requirements for the award of the degree of MASTER OF SCIENCE and submitted in the DEPARTMENT OF BIOSCIENCES AND BIOMEDICAL ENGINEERING, Indian Institute of Technology Indore, is an authentic record of my own work carried out during the time period from August 2023 to May 2025 under the supervision of Dr. Abhijeet Joshi, Associate professor, IIT Indore.

The matter presented in this thesis has not been submitted by me for the award of any other degree of this or any other institute.

Milan khanda 20/5/25 Signature of the student with date

Milan Khanda

This is to certify that the above statement made by the candidate is correct to the best of my/our knowledge.

Signature of the supervisor of the thesis with date

Dr. Abhijeet Joshi

Milan Khanda has successfully given his/her M.Sc. Oral Examination held on 7th May, 2025.

Signature of Supervisor of the MSc thesis

Date: 10/125

Convener, DPGC

Date: 20/05/2025

ACKNOWLEDGEMENTS

I would like to take this opportunity to express my heartfelt gratitude to all those who have supported and guided me throughout my master's thesis journey.

First and foremost, I extend my most profound appreciation to my supervisor, **Dr. Abhijeet Joshi**, whose invaluable guidance, encouragement, and insightful feedback have been instrumental in shaping the course of this research. In the research project, his constant incredible ideas and liberation at work are truly inspiring and motivate me to pursue research and academics. His unwavering support and dedication provided the foundation for my academic growth and inspired me to pursue excellence at every stage. This is one of my great journeys in life under his supreme supervision.

I am sincerely grateful to my mentor, **Simran Rana**, whose skills, wisdom, and constructive advice helped me navigate challenging moments and broaden my perspective on scientific research. She is always helpful in guiding me in experiments, making out any complex theories easily, and in presentation making, etc. Thank you so much for your constant motivation, dedication, and encouragement. I wish to acknowledge **Badri Narayan Sahoo**, an excellent mentor and PhD scholar in our laboratory, whose research skills, technical expertise, and willingness to share knowledge enriched my learning experience and contributed significantly to the progress of this work. Thank you so much for your constant guidance.

I am grateful to have seniors like **Tileshwar Sahare** and **Surbhi Jaiswal** for their valuable support and assistance during the journey. I also want to express my gratitude to **Pallabi Seal**, **Sagnik Mitra**, and **Aritra Chakraborty** for their constant support and help in this journey.

I would like to thank **Prof. Sharad Gupta** for providing the IR thermal camera for my experiments. In this regard, I want to acknowledge **Anusha Srivastava** for her teachings and assistance.

I would like to thank **Dr. Sunil Kumar Boda, IIT Madras,** for continuously guiding and motivating me to publish papers. Finally, we have recently published a peer-reviewed paper that inspires me to engage in research.

I would like to thank our HOD, **Dr. Parimal Kar**, for his constant motivation, support, and guidance throughout the journey. I acknowledge all the professors, **Department of Biosciences and Biomedical Engineering at IIT Indore,** for fostering an intellectually stimulating environment and for their encouragement throughout my studies. My appreciation also extends to the **BSBE office** and all staff members, whose assistance with instrumentation and experimental procedures was invaluable.

I am also thankful to the **SIC Facility** at IIT Indore for providing the necessary equipment and infrastructure to successfully complete this research. Finally, I acknowledge the **Indian Institute of Technology Indore** for offering an inspiring academic environment and the opportunity to pursue my research aspirations.

To my friends, Soumalya, Mahesh, Md Belal, Nandini, Shubhi, Ritika, Rishi, Deveish, and Omkar, thank you for your constant encouragement and understanding, and for making this journey memorable with your companionship. My deepest gratitude goes to my family, my parents (Mr. Pintu Khanda and Mrs. Sandhya Rani Khanda) for their unconditional love, patience, and belief in me; their support has been my greatest strength.

Dedicated to Ramakrishna Math and Ramakrishna Mission, Belurmath

Abstract

Breast cancer treatment presents significant medical challenges globally. Traditional treatments are available, but leave serious side effects. Therefore, advanced and innovative approaches are urgently required for effective therapeutic treatments. This research focuses on developing NIRresponsive thin films for enhanced chemo-photothermal therapy in treating oral cancer. The approach involves synthesizing iron oxide nanoparticles (IONPs), Prussian blue nanoparticles (PBNPs), and Prussian blue-coated iron oxide nanoparticles (PB@IONPs), which are then incorporated into sodium alginate-based thin films. These films are designed to improve drug delivery and photothermal efficiency under NIR laser exposure. The drug used is 5-fluorouracil (5-FU), which is known for killing rapidly dividing cancer cells. In vitro studies show controlled drug release without laser exposure and a burst release with NIR laser irradiation. Notably, PBNPs and PB@IONPs-loaded thin films exhibit superior photothermal efficiency and drug release kinetics compared to IONPs. The nanoparticles are found to be biocompatible, and the thin films demonstrate promising photothermal efficiency with sustained release without laser exposure and burst release, providing a promising platform for advanced breast cancer therapy.

Keywords: Thin film, NIR-responsive nanoparticles, drug delivery, Photothermal therapy, breast cancer.



LIST OF PUBLICATIONS

From Thesis

 NIR-responsive thin film for effective chemo-photothermal drug delivery in the treatment of oral cancer (manuscript preparation).

Apart from Thesis

- Khanda, M.; Seal, P.; Mohan, A. J.; Arya, N.; Boda, S. K. Antimicrobial Peptides and Their Application to Combat Implant-Associated Infections Opportunities and Challenges. Nanoscale 2025, 17 (17), 10462—10484.

 https://doi.org/10.1039/D5NR00953G.
- T Sahare, S Rana, B Sahoo, **Milan Khanda**, A Joshi, "Smartphone-Based Colorimetric Detection of Urinary Glucose Using a Novel Green and Red/Green Approach" (Revision submitted). (Manuscript ID: BIOSX-D-24-00209)



TABLE OF CONTENTS

LIST OF FIGURES

NOMENCLATURE

ACRONYMS	.xxi
Chapter 1	1
Introduction	1
Chapter 2	5
Literature Review	5
Chapter 3	7
Objectives of the project	7
Chapter 4	8
Materials and Methodology	8
4.1. Materials	8
4.2. Methods	8
4.2.1. Synthesis of Iron Oxide Nanoparticles	8
4.2.2. Synthesis of Prussian blue nanoparticles	8
4.2.3. Synthesis of Prussian blue-coated iron oxide nanoparticle	8
4.2.4. Characterization of nanoparticles	9
4.2.5. Photothermal efficiency of nanoparticles	9
4.2.6. Preparation of thin films	10
4.2.7. Characterization of thin film	10
4.2.8 Photothermal efficiency of thin film	10

	4.2.9. IR imaging by thermal camera	.10
	4.2.10. Nanoparticle release profile	.11
	4.2.11. Swelling index of thin film	.11
	4.2.12. Drug encapsulation efficiency of thin films	.11
	4.2.13. Drug release kinetics of thin film	.11
	4.2.14. Laser-induced drug release.	.13
	4.2.15. <i>In vitro</i> cytotoxicity	.13
	4.2.16. Live-dead assay	.13
	4.2.17. ROS and apoptosis study	14
C	hapter 5	.14
R	esult and discussions	.14
	5.1 Characterization of Iron Oxide Nanoparticles	.14
	5.1.1. Absorbance in UV-vis spectrometer	.14
	5.1.2. Magnetic properties of iron oxide nanoparticles	.14
	5.1.3. FE-SEM images of IONP	.15
	5.1.4. Zeta potential	.15
	5.1.5. XRD analysis	.15
	5.2 Characterization of Prussian Blue Nanoparticles	.16
	5.2.1. Absorbance spectra in UV-vis spectrometer	.16
	5.2.2. FE-SEM images and EDAX report of PBNP	16
	5.2.3. Zeta-potential	17
	5.2.4. XRD analysis	.18
	5.3. Characterization of Prussian blue coated iron oxide nanoparticles.	18
	5.3.1. Absorbance spectra in UV-vis spectrophotometer	.18
	5.3.2. FE-SEM images and EDAX report of PBIONP	.19

5.3.3. Zeta-potential	19
5.3.4. XRD analysis	20
5.4. Characterization of thin films	21
5.4.1. Solubility in water	22
5.4.2. FE-SEM images and EDX of thin films	22
5.4.3. XRD analysis of thin films	22
5.4.4. AFM of thin films	23
5.4.5. Swelling index of thin films	24
5.5. Photothermal efficiency of nanoparticles	25
5.6. Photothermal efficiency of thin films	26
5.6.1. IR-thermal imaging	27
5.7. Characterization of 5-fluorouracil	29
5.7.1. Absorbance spectra of drug	29
5.7.2. Calibration curve of drug	29
5.8. Drug-encapsulation Efficiency	30
5.9. <i>In vitro</i> drug release profile	31
5.10. Nanoparticle release profile	31
5.11. In Vitro cytotoxicity of nanoparticles and drug	40
5.12. Live-dead assay using chemo-photothermal therapy	43
5.13. ROS study in cells.	46
5.14. Apoptosis study on cells	47
Chapter 6	50
Conclusions	50
References	52



LIST OF FIGURES

Figure 1.1: Schematic representation of thin film-mediated drug delivery in
treating breast cancer using Chemo-photothermal effect under NIR
laser
Figure 5.1: The absorption spectrum graph of iron oxide nanoparticles shows a broad peak at the NIR range
Figure 5.2: Iron oxide nanoparticles show a magnetic attraction toward a magnetic bar
Figure 5.3: FE-SEM images of IONP and its particle size distribution curve
Figure 5.4: Zeta potential of IONP
Figure 5.5: XRD peak of IONP at corresponding 2Θ16
Figure 5.6: The absorption spectrum graph of Prussian blue nanoparticles showing its peak at around 708 nm
Figure 5.7: FE-SEM images and EDX report of PBNP17
Figure 5.8: Zeta potential of PBNP
Figure 5.9: XRD peak of PBNP at the corresponding 2Θ peak 18
Figure 5.10: The absorption spectrum graph of Prussian blue-coated nanoparticles
Figure 5.11: FE-SEM images and EDX report of PB@IONP19
Figure 5.12: Zeta potential of PBNP20
Figure 5.13: XRD neak of PR@IONP at corresponding 20

Figure 5.14: Observation of thin film's solubility in water and crosslinking
step
Figure 5.15: FE-SEM images and EDX of thin films
Figure 5.16: XRD images of thin films
Figure 5.17: 3D AFM images of thin films24
Figure 5.18: Swelling index of all thin films immersed in 1 ml DI solution
Figure 5.19: The graph of temperature rise in IONP, PBNP, and PB@IONP under 808 nm NIR laser
Figure 5.20: Graphical representation of temperature rise in IONP, PBNP & PB@IONP-loaded thin films in 1 ml and 200µl solution
Figure 5.21: Thermal image of all four thin films by the exposure to NIR 1 W, 808 nm laser for 5 minutes by using an IR thermal imaging camera28
Figure 5.22: The maximum absorbance peak of 5-FU at 266 nm 29
Figure 5.23: Calibration curve and retention time of 5-FU analyzed by HPLC
Figure 5.24: Final drug encapsulation efficiency of thin films30
Figure 5.25: The drug release percentage from SA+D, IONP, PBNP, and PB@IONP-loaded thin films without laser exposure and with laser exposure
Figure 5.26: The NPs release profile from IONP, PBNP, and PB@IONPloaded thin films
Figure 5.27: MTT assay of PBNP & PBIONP nanoparticles in HEK 293 & MCF-7 cell line.

Figure 5.28: In vitro cytotoxicity assay of 5-FU and PBIONP IN MCF-7
and SCC-9 cells using Alamar blue assay
Figure 5.29: Live and Dead cell analysis- Fluorescence image of live and
dead analysis by fluorescent microscopy by treating MCF-7 cells with Thin
films
Figure 5.30: Live and Dead analysis using multiple PBIONP TF in MCF-7
cells
Figure 5.31: ROS production studies in cells treated with thin films under
laser exposure and drug release conditions
Figure 5.32: Apoptosis studies in cells treated with thin films under laser
exposure and drug release conditions. The annexin V color intensity graph
was calculated. 38

NOMENCLATURE

Acronym 5-Fluorouracil 5-FU Nanoparticles NPs Photothermal Therapy PTT Iron oxide nanoparticles **IONP** Reactive Oxygen Species **ROS** Sodium alginate SA Prussian blue nanoparticles **PBNP** Prussian blue coated iron oxide nanoparticles PB@IONP Near Infrared **NIR** Field emission scanning electron microscopy **FESEM** X-ray diffraction XRD Atomic Microscopy **AFM**

Expansion

3,4,5-(dimethylthiazol-2-yl)-2,5 diphenyltetrazol MTT

Dimethyl sulphoxide

2',7'-dichlorofluroscein diacetate **DCFDA**

Glycylphenlyalanyl aminoflurocoumarin **GF-AFC**

Propidium iodide PΙ

DMSO

Confocal microscopy laser scanning **CLSM**



ACRONYMS

Sign Meaning λ Wavelength μ Micron °C Degree Centigrade μl Microlitre ml Millilitre nm Nanometer nMNanomolar $\mu g/ml$ Microgram per millilitre mins Minutes hrs Hours R^2 Regression coefficient W % Watt Percentage



Chapter 1

Introduction

Cancer is a complex group of diseases characterized by an uncontrolled cell cycle and the potential to metastasize to other parts of the body. It is the top-leading cause of mortality in the world. There are 20 million new cases of cancer in 2022, and 9.7 million deaths from cancer worldwide¹. Research in cancer aims to understand the underlying mechanisms, develop effective treatments, and ultimately find a cure. The deadliest cancers are breast cancer, prostate cancer, lung cancer, oral cancer, colorectal cancer, skin cancer, etc. Breast cancer is the leading cancer worldwide, responsible for more than 6,70,000 deaths in 2024. Females are more prone to this deadliest cancer. Approximately 99% of breast cancers occur in women, and 0.5–1% of breast cancers occur in men ². Certain risk factors for breast cancer include increasing age, obesity, use of alcohol, family history of breast cancer, history of radiation exposure, reproductive history (such as menarche and menopause), tobacco use, and postmenopausal hormonal therapy. Approximately half of breast cancers develop in women who have no signs or symptoms and are over 40 years old. Certain inherited high-penetrance gene mutations greatly increase breast cancer risk, the most dominant being mutations in the genes BRCA1, BRCA2, and PALB-2 3. Specific inherited genetic mutations, such as BRCA1 and BRCA2, significantly increase the risk of breast cancer. Higher levels of estrogen and progesterone can increase the risk. Factors like early menstruation, late menopause, and hormone replacement therapy may influence this. Researchers are working to improve response rates and overcome resistance to these therapies. Traditional chemotherapy and radiotherapy, while effective, often come with significant side effects and limitations in targeting cancer cells precisely. The chemotherapy method uses drugs to kill rapidly dividing cancer cells. It can also harm healthy cells, leading to side effects like nausea, hair loss, and fatigue ⁴. Radiotherapy uses high-energy radiation to destroy cancerous cells. It may damage surrounding healthy tissues,

causing skin irritation, fatigue, and other side effects. In traditional surgical methods, physicians remove the tumor cells or tissue physically. However, it is invasive, with risks of infection and complications, and not always feasible for aggressive or metastasized cancers ⁵. Therefore, researchers are continuously finding suitable alternative methods for effective cancer treatment.

Photothermal therapy (PTT) is an innovative alternative to cancer treatment that leverages the photothermal effect, where light energy is converted into heat to destroy cancer cells selectively⁶. This method is particularly promising for topical cancer due to its minimally invasive, precise targeting and fewer side effects than traditional methods. In PTT, a photothermal agent is introduced to the target area. When exposed to a specific wavelength of light, these agents absorb the light and convert it into heat, increasing the temperature of the cancerous tissue to a level that induces cell death. This localized heating minimizes damage to surrounding healthy tissues. Nanotechnology has been a promising tool in clinical healthcare, which has resulted in the development of nano- or micro-carriers for diagnosis, imaging, and drug delivery in various diseases like cancers. The primary goal is to deliver a drug and release it in a controlled manner at a particular site, i.e., cancerous cells or tissue. This can be achieved effectively by using nanocarriers. Generally, nanoparticles are small colloidal molecules that are less than 1000 nm in size. The intended nanocarriers are highly biodegradable and biocompatible, with minimum cytotoxicity and stable accumulation in the target tissue 7 .

Recent advancements in PTT involve using nanoparticles, especially near-infrared responsive ones, such as gold nanoparticles, gold nanorods, magnetic nanoparticles, Prussian blue nanoparticles, and polydopamine nanoparticles, which have excellent photothermal conversion efficiency and advanced imaging compatibility ⁸. Among them, magnetic nanoparticles and Prussian blue nanoparticles are extensively used as effective photothermal agents in cancer. However, iron oxide

nanoparticles are highly prone to aggregation, highly reactive, have a higher oxidation state, and are susceptible to environmental factors, making them unstable ⁹. Therefore, iron oxide nanoparticles were coated with Prussian blue to prevent this instability and improve the synergistic photothermal effect. Coating PB onto magnetic nanoparticles (MNP) is possible by reacting hexacyanoferrate (II) with ferric ions in the presence of MNP, though acidic conditions are preferred for better coating efficiency due to the creation of Fe³⁺ sites on the MNP surface ¹⁰. PTT can also be synergistically combined with other therapies, such as immunotherapy or chemotherapy, to enhance the overall efficacy of the treatment. This photothermal effect facilitates controlled drug release and directly induces hyperthermia in cancer cells, leading to their apoptosis or necrosis. Among the epithelial cancer drugs, the FDAapproved drug 5-fluorouracil (5-FU) is extensively used for breast cancer ¹¹. It can inhibit DNA replication, disrupt RNA, and arrest the cell cycle, making it an ideal therapeutic agent for cancer treatment. It also has intrinsic fluorescence properties for better visualization. By leveraging the dual functionality of photothermal therapy and controlled drug release, this approach aims to enhance the therapeutic efficacy against breast cancer while reducing systemic cytotoxicity and adverse side effects.

Polymeric thin films are versatile materials composed of polymers that can be tailored for various applications, particularly in drug delivery. Various polymers are extensively utilized in the fabrication of thin films, particularly for applications in drug delivery ¹². These polymers are polyvinyl alcohol (PVA), poly-lactic acid (PLA), polycaprolactone (PCL), chitosan, sodium alginate, etc. These films exhibit unique properties such as adjustable thickness, porosity, and biodegradability, enhancing their functionality in effectively delivering drugs. Such films can be engineered to control the drug release rate, ensuring that therapeutic agents are delivered sustainably over a specific period. In cancer treatment, thin films are designed to carry therapeutic agents directly to the tumor site, enhancing the efficacy of the treatment while

minimizing side effects. Their ability to provide controlled and sustained drug release ensures a consistent therapeutic level in the body, which is crucial for effective cancer treatment. Moreover, thin films can be engineered to respond to specific stimuli, such as pH changes, light, or temperature, allowing for targeted and controlled drug release in the tumor site ¹³. This targeted approach can improve the therapeutic outcomes and reduce the systemic toxicity typically associated with conventional cancer therapies. These films utilize several strategies to deliver therapeutic agents effectively in terms of drug release mechanisms. Diffusion-controlled release occurs when the drug gradually diffuses through the polymer matrix 13,14. In contrast, degradation-controlled release relies on the gradual breakdown of the polymer to release the drug over time. Moreover, some films are engineered for environment-responsive release, allowing the release of drugs triggered by specific stimuli such as changes in light, pH, or temperature.

One innovative approach is to incorporate photothermal responsive nanoparticles into the single thin film platform, taking care of its biocompatibility and biodegradability. These nanoparticles absorb nearinfrared (NIR) light, converting it into heat, which triggers the release of the drug from thin films, allowing for precise drug release ¹⁵. The primary strategy of the research project is to incorporate iron oxide nanoparticles, Prussian blue nanoparticles, and Prussian blue-coated iron oxide nanoparticles, and anti-cancer drugs 5-FU into the sodium alginate-based thin film, enabling the system to respond to NIR light, generating localized heat that can trigger the sustained release of encapsulated anticancer drugs to the tumor site. These approaches offer less invasive, highly targeted treatment options tailored to individual patient needs, potentially transforming breast cancer treatment and improving patient outcomes. The successful development of this thin film could pave the way for new, minimally invasive treatments for topical cancer and potentially other types of cancer as well. By advancing

research in these areas, scientists are edging closer to a cure while improving the quality of life of cancer patients.

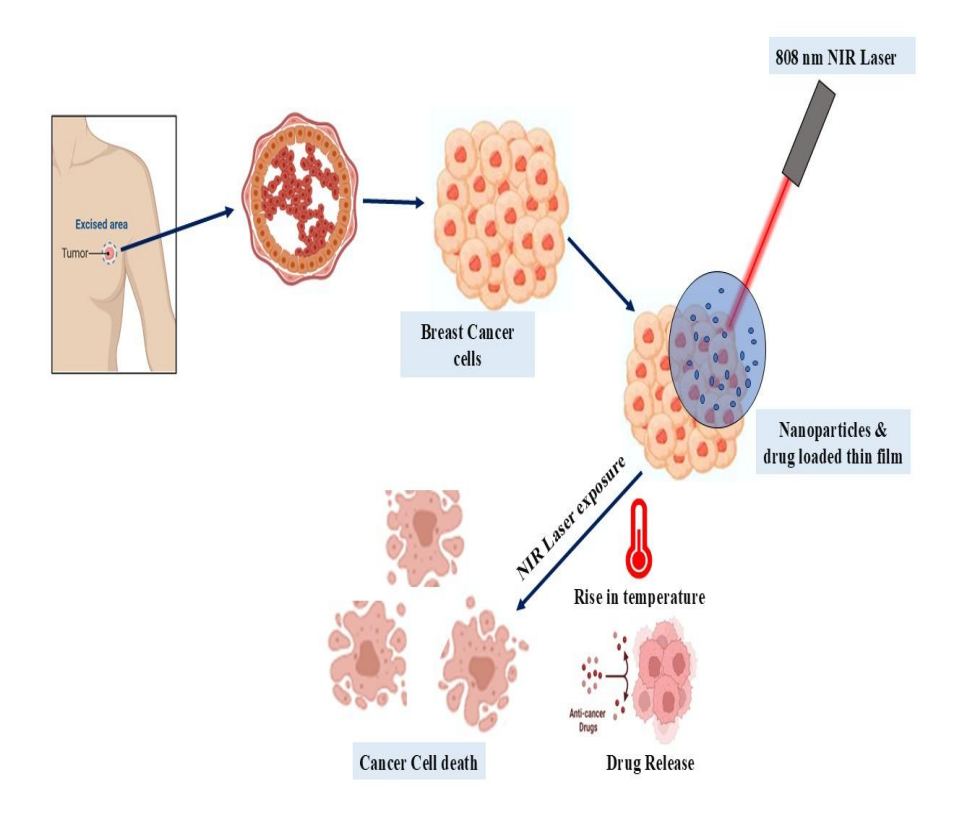


Figure 1.1: Schematic representation of thin film-mediated drug delivery in treating breast cancer using Chemo-photothermal effect under NIR laser exposure.

Chapter 2

Literature review

Integrating near-infrared (NIR) responsive nanoparticles into polymeric thin films for controlled drug delivery in cancer treatment has garnered significant attention in recent years. This literature focuses on using magnetic and Prussian blue nanoparticles in photothermal therapy (PTT) and drug delivery systems.

2.1. <u>Magnetic Nanoparticles as a photothermal agent:</u>

The development of PEGylated iron/iron oxide core/shell nanoparticles (Fe@Fe3O4 NPs) for cancer theranostics, combining magnetic targeting, MRI, and near-infrared (NIR) photothermal therapy (PTT). These nanoparticles demonstrate high photothermal conversion efficiency (~20%), excellent stability, and low toxicity. They outperform gold nanorods in terms of stability under NIR exposure, and their magnetic properties allow for enhanced tumor targeting, improving treatment precision. In both *in vitro* and *in vivo* studies, the nanoparticles effectively ablated cancer cells with minimal damage to healthy tissues, making them a promising tool for cancer treatment ¹⁶.

2.2. Prussian blue nanoparticles as a photothermal agent:

Prussian blue nanoparticles (PBNPs) are another class of NIR-responsive agents that have shown promise in cancer treatment. PBNPs possess excellent photothermal conversion efficiency and biocompatibility, making them suitable for PTT applications. Moreover, PBNPs can be easily synthesized and modified to carry therapeutic agents, allowing for simultaneous drug delivery and photothermal therapy. Research has demonstrated that PBNPs can be integrated into a thin film, resulting in a multifunctional system for controlled drug release and effective cancer treatment ¹⁷.

2.3. Prussian blue coating on magnetic nanoparticles:

One study presents the development of Prussian blue-coated magnetic nanoparticles (PB@MNP) for efficiently removing radioactive cesium (Cs) from contaminated environments. Prussian blue, known for its high cesium adsorption capacity (96 mg Cs/g), is coated onto magnetic nanoparticles, allowing easy recovery through magnetic separation. This coating enhances the nanoparticles' stability and adsorption efficiency. The PB@MNP demonstrates high performance in capturing cesium at both high and low concentrations, making it a promising solution for environmental cleanup and potential medical applications for radiocesium removal ¹⁸.

2.4. 5-Fluorouracil in breast cancer treatment:

One study reviews the efficacy of continuous infusion of 5-fluorouracil (5-FU) in treating breast cancer. Traditionally used in bolus injections, 5-FU has shown promise in continuous infusion, particularly for heavily pretreated patients. Studies indicate that continuous 5-FU increases response rates, with combination chemotherapy yielding response rates as high as 89%. Additionally, prolonged infusion reduces myelotoxicity, allowing for higher cumulative doses. However, new toxicities, such as palmar-plantar erythrodysaesthesia (PPE), have emerged. The paper highlights the pharmacokinetics and metabolism of 5-FU, underscoring the importance of infusion in optimizing drug exposure during tumor cell replication. Clinical trials confirm its effectiveness, though the optimal dose and administration strategy remain under evaluation. The study advocates for further randomized trials to assess continuous 5-FU's role in breast cancer treatment and its potential in combination regimens, particularly in metastatic and adjuvant settings.¹⁹

2.5. Stimuli-responsive thin film-mediated drug delivery:

Various studies represent the development of stimuli-responsive polyelectrolyte multilayer (PEM) films for multi-drug delivery. These films, made from poly(allylamine hydrochloride) (PAH) and poly(methacrylic acid) (PMA), change their morphology in response to environmental stimuli like pH and ionic strength, enabling controlled drug release. The films were loaded with bovine serum albumin (BSA) and ciprofloxacin hydrochloride (CH), showingsustained release for up to 8 hours. The study highlights the potential of these biocompatible films for applications in transdermal drug delivery, antimicrobial coatings on implants, and drug-releasing stents.²⁰

Sodium alginate-based thin film, synthesized through solvent casting on a Petri plate, offers several advantages for drug delivery, including Enhanced Bioavailability, Patient Compliance, Controlled Release, Targeted Delivery, and Non-invasiveness ²¹. Incorporation of NIRresponsive nanoparticles into thin film has enhanced the efficacy of drug delivery systems by providing controlled and sustained release of drugs in response to NIR-laser exposure. Studies have highlighted the potential of thin film-based systems in improving the therapeutic outcomes of cancer treatments. Combining magnetic nanoparticles, Prussian blue nanoparticles, and Prussian blue-coated iron oxide nanoparticles along with drug in a thin film represents a novel approach to cancer therapy. This dual-functional system leverages the advantages of both types of nanoparticles, providing enhanced photothermal effects and controlled drug release. Recent research has explored the synergistic effects of combining these nanoparticles, demonstrating improved therapeutic efficacy in clinical breast cancer models.

Chapter 3

Objective of the project

➤ Development of NIR-responsive thin film loaded with 5-Fluorouracil for effective chemo-photothermal therapy in breast cancer treatment.

Chapter 4

Materials and methodology

4.1. Materials:

Ferric chloride (Rankem, India), Ferrous sulfate (Rankem, India), Sodium hydroxide, Potassium hexaferrocyanide (Loba Chemie), sodium alginate (Loba Chemie), glacial acetic acid (EMPARTA, India), Polyvinylpyrrolidone (PVP) (Sigma Aldrich), calcium chloride (SRL), 3-(4,5-Dimethylthiazol-2-yl)-2,5-Diphenyltetrazolium bromide (MTT), dimethyl sulphoxide (DMSO) from Sigma-Aldrich Chemicals Ltd. (St. Louis, MO, USA). Dulbecco's modified Eagle media, antibiotics, Fetal Bovine Serum, Trypsin, PBS, and all other cell culture reagents from Himedia, Propidium Iodide, Annexin V (from Thermo Fisher Scientific), Glycylphenylalanyl-aminocoumarin (GF-AFC) from Promega Pvt. Limited.

4.2. Methods:

4.2.1. Iron-oxide nanoparticles (IONP) synthesis:

The iron oxide nanoparticles were synthesized using the co-precipitation approach, which involved mixing 1% (w/v) FeCl₃ and 1% (w/v) FeSO₄ in a beaker in a 2:1 ratio. The beaker was then placed on a magnetic stirrer set to 500–700 rpm. The pH was then kept at 12 by gradually adding 5 M NaOH. The suspension was heated at 80 to 90° Celsius for two hours after the pH was kept at 12. The suspension was centrifuged for 15 minutes at 5000 rpm three times using pure ethanol. After that, the pellet was dried in a lyophilizer and kept for future additional characterization and analysis.²²

4.2.2. Prussian blue nanoparticle (PBNP) synthesis:

The Prussian blue nanoparticles were synthesized using the coprecipitation method. 3.5% (w/v) polyvinylpyrrolidone (PVP) was added to 15 mL of distilled water. A 0.63% (w/v) potassium ferrocyanide was added to the solution under a magnetic stirrer, and pH 4-4.5 was maintained. Equimolar concentrations, i.e., 0.63% (w/v) of FeCl₃, were added to get Prussian blue precipitation. PVP is a stabilizing and reducing agent crucial for Prussian blue nanoparticle synthesis. Then, the suspension was washed thrice with distilled water by centrifugation for 15 minutes at 8000 rpm. The pellet obtained was then lyophilized and kept for future analysis.²³

4.2.3. Prussian blue coated-iron oxide nanoparticles (PB@IONP) synthesis:

Prussian blue can be coated onto iron oxide nanoparticles through the chemical interaction method. Firstly, 50 ml of 10 mm potassium ferrocyanide solution was prepared in distilled water. The mixture was continuously stirred for 20 min. Iron oxide nanoparticles were added to the mixtures, pH 2-3 was maintained by 100 mM HCl, and the mixtures were kept for 1-2 hours at 50°C for effective coating. Then, the suspension was washed thrice with distilled water by centrifugation for 15 minutes at 10000 rpm. The pellet obtained was then lyophilized and kept for future analysis.²⁴

4.2.4 Characterization of nanoparticles:

The size and morphology of the synthesized nanoparticles were analyzed using field emission scanning electron microscopy (FE-SEM). The sample of iron oxide, Prussian blue, and Prussian blue-coated iron oxide nanoparticles was synthesized, and FE-SEM images were taken. The elemental composition of nanoparticles was confirmed by the Energy Dispersive X-ray spectroscopy (EDX). Similarly, it also confirmed the Prussian blue coating on magnetic nanoparticles. The zeta potential was

measured using Anton Paar Litisizer equipment for surface charge analysis.

X-ray diffraction (XRD) was also used for the characterization of nanoparticles, which provides information regarding the crystal structure and elemental composition. The sample was taken in powdered form. The composition of particles was confirmed by comparing the position and intensity of the peaks with the standard reported available data.

4.2.5. Photo-thermal efficiency of nanoparticles:

The photo-thermal efficiency of IONP, PBNP, and PB@IONP was analyzed by exposing the particles dissolved in 1 ml of distilled water to an 808 nm, 1 W Near-infrared (NIR) Laser. First, all the nanoparticles were exposed to a constant pulse (1 pulse) of 808 nm, 1W for different time intervals (0 min, 2.5 min, 5 min, 7.5 min, and 10 min). The rise in temperature was recorded in the thermocouple as occurring due to NIR laser exposure. Here, we have taken two concentrations of nanoparticles: 5 mg/ml and 500 μ g/ml for photothermal efficiency. The reason behind taking 500 μ g/ml nanoparticles was that the experimental concentration of nanoparticles loaded on a small thin film was 500 μ g/ml.

4.2.6. Preparation of thin film:

Sodium alginate (SA) was completely dissolved in distilled water under a continuous stirrer at 40 °C for 3-4 hours. The concentration of SA is 4% (w/v), i.e., 0.4 g of SA was taken in 10 ml of distilled water. During the mixing, nanoparticles were added to the solution. After being evenly distributed, the solution was cast on 30 mm Petri plates. The petri plates were allowed to dry at room temperature for 12-15 hours. After drying up, the thin film was peeled off the Petri plate and punched off to get a small thin film and stored for future work.²⁵

4.2.7. Characterization of thin film:

The synthesized thin film was characterized by field emission scanning electron microscopy (FE-SEM), which confirmed the surface morphology and alignment of the film. It confirms the presence of nanoparticles embedded in the thin film. Further, elemental compositions were analyzed through EDX and XRD. Atomic Force Microscopy (AFM) was used to analyze the surface topology and surface roughness of the synthesized thin films. It also confirmed the alignment of nanoparticles on the thin film.

4.2.8. Photo-thermal efficiency of thin film:

The photothermal efficiency of IONP, PBNP, and PB@IONP loaded thin film was checked by exposing 808 nm, 1 W NIR laser. First, one small thin film was checked at various time points (0, 2.5, 5, 7.5, 10 mins) with 1 W pulse, and the temperature was recorded with a thermocouple. Secondly, small, thin films immersed in 200 µl distilled water in a 96-well plate were checked for photothermal efficiency, and temperature rise was recorded.

4.2.9. Infra-red imaging using NIR thermal camera:

Temperature rise was analyzed in thin films, kept in a 96-well plate with $200 \,\mu l$, while exposing the thin films to an NIR laser (1 W, 808 nm) for 5 min, which was checked with an NIR thermal camera. The experiment was done in a dark room at room temperature. The temperature change was visualized by a thermogram generated by the NIR thermal camera (Fluke PT i120).

4.2.10. Nanoparticle release profile:

The nanoparticle release profile study, as was the drug release study, was crucial for effective photothermal therapy. For the study, all thin films are exposed to a laser time-dependent manner, like laser-induced drug release. On the other hand, the solution of immersed thin film was checked for intermittent time intervals (1 hr, 6 hrs, 12 hrs, 24 hrs, 48 hrs),

simultaneously done without laser-induced drug release. This was done through a UV-vis spectrophotometer, and based on the corresponding peak, it confirmed the release of nanoparticles.

4.2.11. Swelling index:

The swelling index was studied by measuring the percentage of water uptake by the thin films ²⁶. Accurately weighed dry crosslinked thin films were taken in an MCT containing 1 ml of water and allowed to stand for up to 60 minutes. The excess liquid retained on the thin films was removed with filter paper, and the swollen thin films were weighed again. The experiments were performed in a biological triplicate manner. The swelling index of the thin films was calculated by using the formula:

Swelling index = $\underbrace{\text{(weight of swollen thin film - initial weight of dry thin film)}}_{\text{initial weight of dry thin film}} \times 100$

4.2.12. Drug encapsulation efficiency in the thin film:

The entire thin film is dissolved in 1 ml of distilled water in order to completely degrade and obtain the drug encapsulation efficiency in the thin film. The dissolved solution was centrifuged, and the sodium alginates were deposited as a pellet. The drugs were in supernatant, measured at 266 nm in a UV-vis spectrophotometer, and the drug encapsulation efficiency was calculated. As the drug can be present on the surface of the thin films while dipping in CaCl₂ solution, the surface-associated drug leaches out into the solution. The UV-visible spectrum was measured, and the final drug encapsulation efficiency of each thin film was calculated after the crosslinking step.

4.2.13. *In vitro* drug release study:

An *in vitro* drug release study was used to determine the amount of the drug released from the thin films at different time intervals (2.5, 5, 7.5, and 10 mins). The drug-loaded thin films were suspended in 10 ml of distilled water and kept on a magnetic stirrer at 200 rpm and 37°C. Then, 1 ml of sample was withdrawn at different intervals by replacing it with

fresh 1 ml DI. The readings of the withdrawn samples were taken using an HPLC at 266 nm, and then the percentage of drug release was calculated.

4.2.14. Laser-induced drug release study:

For the laser-induced drug release study, thin films were placed in 1 ml DI containing MCT and exposed to a 1W, 808 nm laser in a time-dependent manner. After each specific time, the laser-exposed thin film was removed, and the sample was stored for the drug release study. All the samples were tested in HPLC to determine the drug release kinetics, and the graph for the same was plotted.

4.2.15. *In vitro* cytotoxicity test:

Biocompatibility or MTT assay of synthesized nanoparticles was done on human embryonic kidney cell line HEK-293 and breast cancer cell line MCF-7. The cells were plated at 8×10^3 cells/well and subsequently incubated at 37°C with 5% CO₂. After 24 h, various concentrations (0.00, 10, 50, 100, 200, and 400 µg/ml) of extraction media replaced the old culture media. Then, after 48 h, MTT reagent was added to each well of a 96-well plate and incubated further for 3h. DMSO was added, and optical density was measured on a plate reader at 570 nm. The IC₅₀ of 5-FU was also determined on the MCF-7 cell line. All the experiments were done in a biological triplicate manner.

4.2.16. Live and Dead cell analysis:

The Live and Dead cell assay was done to check the number of live and dead cells after treating MCF-7 with synthesized thin films. Around 7,000 cells per well were seeded in 24-well plates and allowed to grow in complete DMEM media with 10% FBS and 1% antibiotics. Only nanoparticles and nanoparticle-drug-loaded thin films were kept in the centre of each well plate and were exposed to a 1 W, 808 nm NIR laser for 5 minutes. The intact thin film was incubated for 30 minutes and then removed. The whole plate was incubated for 6 hr. Then, for live cell and

dead cell analysis, glycylphenylalanyl-aminofluorocoumarin (GF-AFC) and propidium iodide (PI) were used, respectively. The spent medium containing the dead cells was collected in MCTs from the respective wells and centrifuged at 600 g for 10 minutes. In the meantime, for the staining of live cells, the GF-AFC stock was added to the assay buffer at a 1/1000 dilution and supplemented to the cells. After the centrifugation of dead cells, the supernatant was removed gently, and 10 μ g/ml of PI was added. Both cell populations were mixed and allowed to incubate for 20 minutes. Then the fluorescent cells were visualized by a fluorescence microscope (Invitrogen by Thermo Fisher Scientific) using emission spectra 505-535 nm. Also, a similar experiment was conducted for multi-thin film-mediated chemo-photothermal cell death, and images were taken.

4.2.17. Reactive Oxygen Species (ROS) & Apoptosis studies:

Similarly to the live-dead cell assay, an Apoptosis and ROS production study was conducted on the thin film and laser-treated cells in two different sets. The ROS study was determined using 2',7'-Dichlorodihydrofluorescein diacetate (DC-FDA) stain, and the apoptosis was studied through Annexin V stain and co-stained with propidium lodide (PI). The spent media contained in each well was discarded, and $10\,\mu\text{g/ml}$ DC-FDA was added to each well and incubated for 20 minutes. Similarly, for apoptosis, $10\,\mu\text{g/ml}$ annexin V and $10\,\mu\text{g/ml}$ PI stain were added, and the plate was allowed to incubate. Then, the ROS-producing and apoptotic fluorescent cells were visualized through fluorescence microscopy.

Chapter 5

Results and discussions

5.1. Characterization of IONP nanoparticles

5.1.1. Absorbance in UV-vis spectrophotometer:

When the absorbance of synthesized iron oxide nanoparticles was taken using a UV-visible spectrophotometer, a broad spectrum was observed from 200 nm to 800 nm. Since the IONP has a broad spectrum and blackish brown compound, therefore, it is highly used for photothermal therapy.

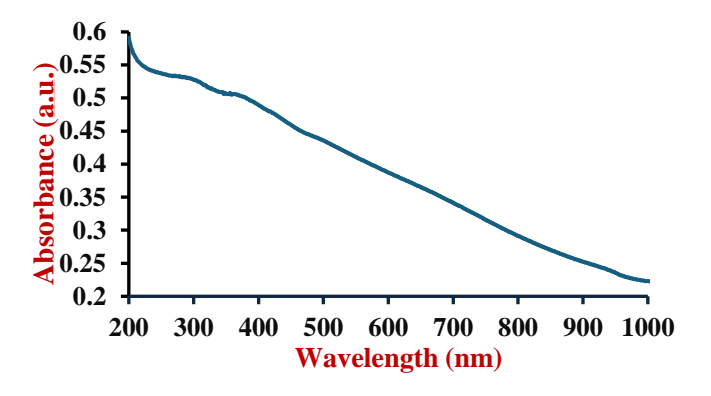


Figure 5.1: The absorption spectrum graph of iron oxide nanoparticles shows a broad spectrum (200-900 nm) in the NIR region.

5.1.2. Magnetic properties of iron-oxide nanoparticles:

The magnetic properties of iron oxide nanoparticles were seen when a magnetic bead was placed near the particles; the nanoparticles were attracted and formed a cluster towards the bead, as seen in **Figure 5.2**.



Figure 5.2: Iron oxide nanoparticles show a magnetic attraction toward a magnetic bar.

5.1.3. FE-SEM images of IONP:

IONP was characterized through Field Emission Scanning Electron Microscopy (FE-SEM) at the Sophisticated Instrumentation Centre, IIT Indore. The result showed that the diameter of the particles is 16.7 ± 1.2 nm and well distributed under the accelerating voltage of 5 kV and a working distance of 5.6 mm.

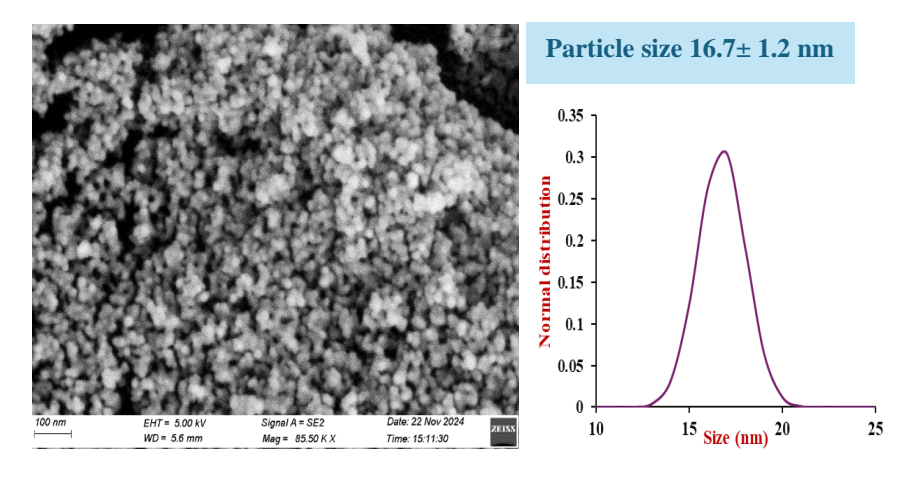


Figure 5.3: FE-SEM images of IONP and particle size distribution curve derived from ImageJ Software.

5.1.4. Zeta-potential:

Zeta-potential of the nanoparticles was measured for 20 cycles. Based on the relative frequency, the zeta potential of IONP is - 29.49 mV, and the standard deviation is 2.31 mV.

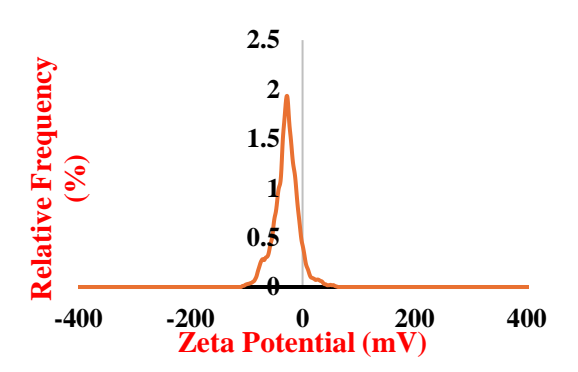


Figure 5.4: Zeta-potential of IONP suspended in DI water.

5.1.5. XRD analysis:

X-ray Diffraction (XRD) of Iron oxide nanoparticles was done at the Department of Metallurgy and Materials Science, IIT Indore. The angle of diffraction (2Θ) was set as 20° to 80° . The XRD peak at 2Θ of the nanoparticles was 30.1° , 35.5° , 42.6° , 57.0° and 64.1° . The peak was analyzed and verified using previously published data. 27

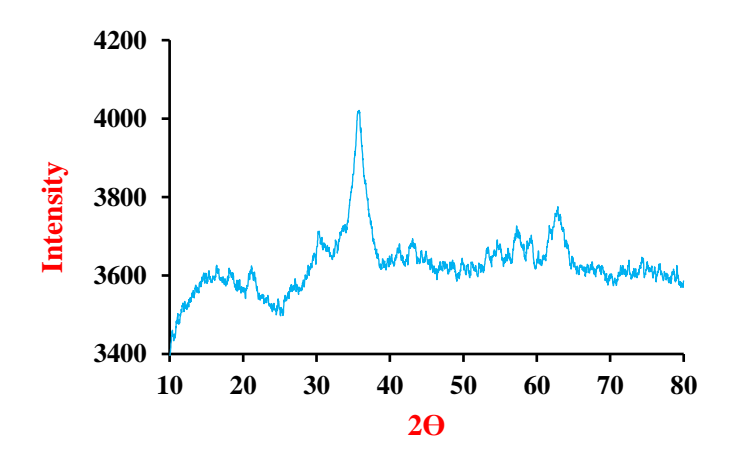


Figure 5.5: XRD peak of IONP at corresponding 2Θ, depicts the crystalline nature of the nanoparticles.

5.2. Characterization of prussian blue nanoparticles:

5.2.1. Absorbance in UV-vis spectrophotometer:

The absorbance graph of Prussian blue nanoparticles was taken using a UV-vis spectrophotometer, showing a maximum peak at around 708 nm, a characteristic peak of Prussian blue. The graph depicts Prussian blue nanoparticles were successfully formed.

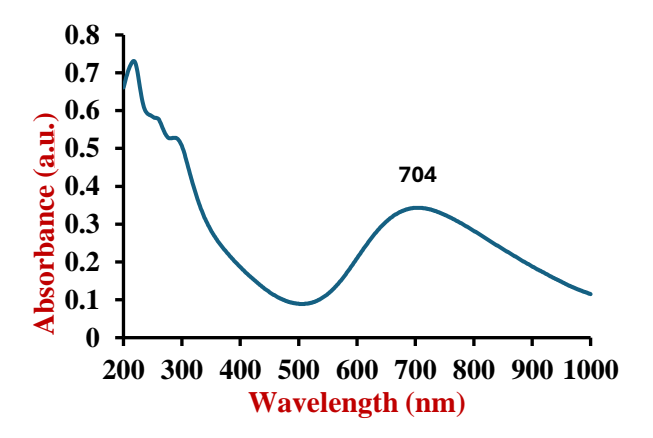


Figure 5.6: The absorption spectrum graph of Prussian blue nanoparticles showing its peak at around 704 nm.

5.2.2. FE-SEM images and EDAX report of PBNP:

PBNP was characterized through Field Emission Scanning Electron Microscopy (FE-SEM) at the Sophisticated Instrumentation Centre (SIC), IIT Indore. The particle size distribution curve showed that the size of the particles is approximately 18.9 ± 3.9 nm and well distributed under the accelerating voltage of 5 kV and a working distance of 5.6 mm. The elemental dispersive X-ray analysis (EDX) shows 38.7% carbon, 41.5% nitrogen, 11.7% iron etc.

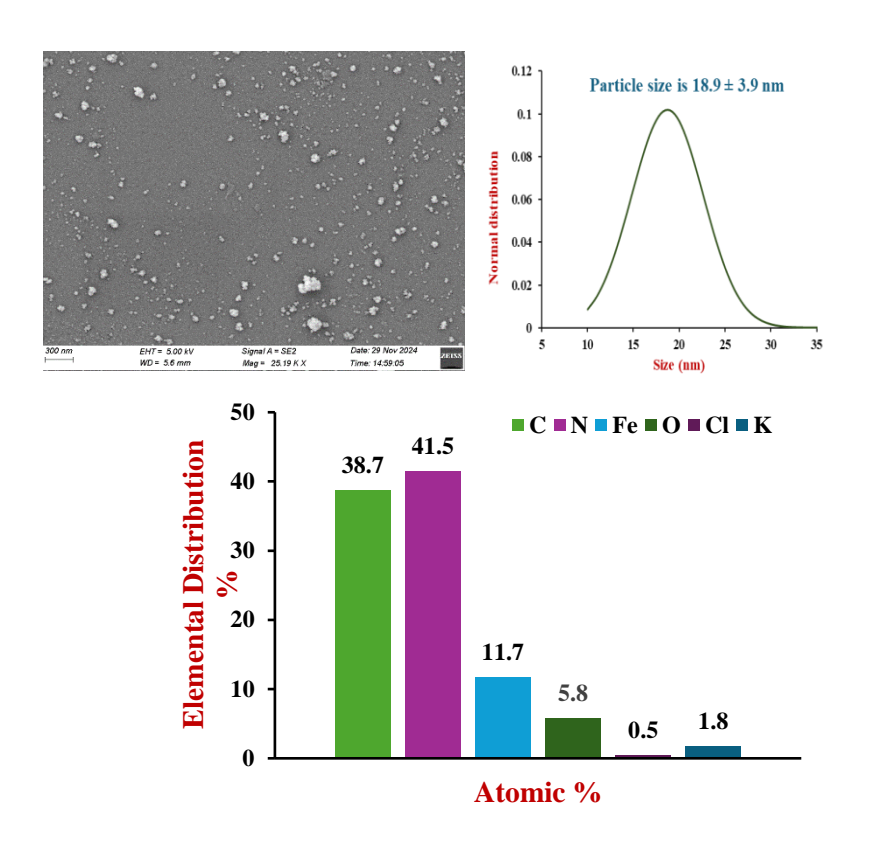


Figure 5.7: FE-SEM images and particle size distribution curve and EDX analysis report of PBNP.

5.2.3. Zeta-potential:

Zeta-potential of the nanoparticles was measured for 20 cycles. Based on the relative frequency, the zeta potential of PBNP is 1.8 mV, and the standard deviation is 2.26 mV. It depicts the low electrostatic repulsive forces between the particles, which tend to aggregate in the solution.

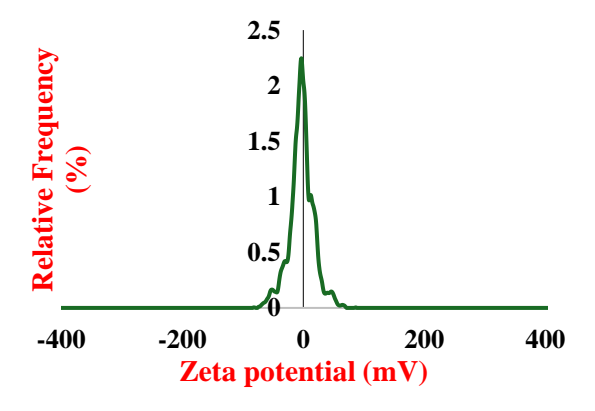


Figure 5.8: Zeta potential of PBNP in DI water.

5.2.4. XRD analysis:

X-ray Diffraction (XRD) of Prussian blue nanoparticles was performed, and the corresponding peak was recorded. The 2 Θ of PBNP is 17.38°, 25°, 39°, 55°, 65°, and 78°. The data was verified with previously published data.²⁸

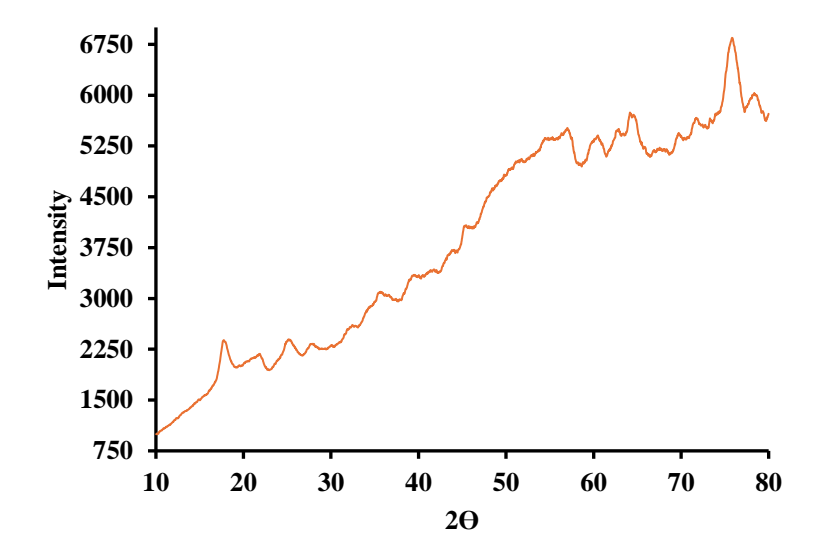


Figure 5.9: XRD peak of PBNP at the corresponding 20 peak.

5.3. Characterization of prussian blue-coated iron oxide nanoparticles

5.3.1. Absorbance in UV-vis spectrophotometer

The absorbance graph of Prussian blue-coated nanoparticles was taken using a UV-vis spectrophotometer, showing a maximum peak at around 783 nm, a characteristic peak of Prussian blue. The graph depicts that Prussian blue coating may be present on iron oxide nanoparticles. The absorption peak at 283 nm may be due to the presence of unreacted FeCl₃.

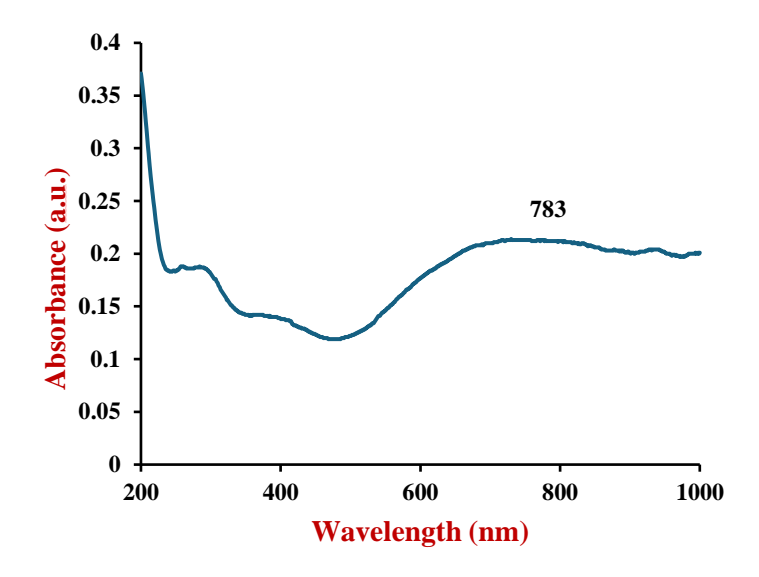
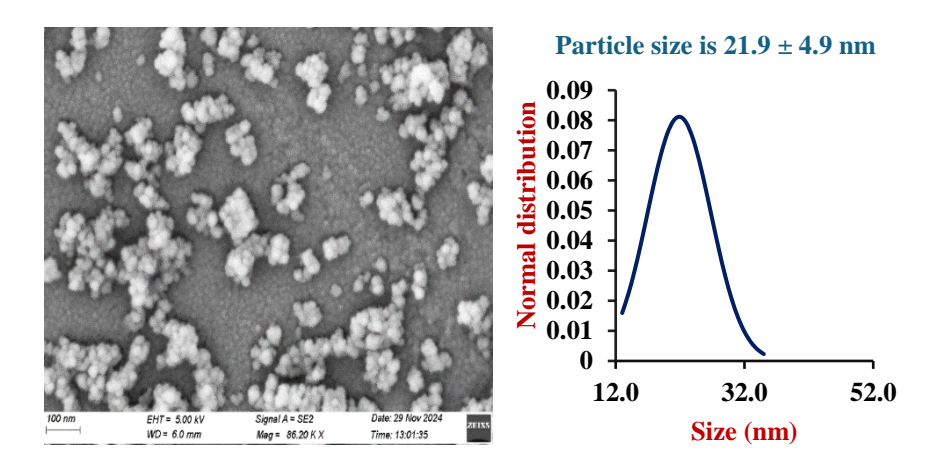


Figure 5.10: The absorption spectrum graph of prussian blue-coated nanoparticles showing itspeak at around 783 nm.

5.3.2. FE-SEM images and EDAX report of PB@IONP:

The characterization of PB@IONP was done through Field Emission Scanning Electron Microscopy (FE-SEM) at the Sophisticated Instrumentation Centre, IIT Indore. The particle size distribution curve showed that the size of the particles is 21.9 ± 4.9 nm and well distributedunder the accelerating voltage of 5 kV and a working distance of 6 mm. The EDX report showed 45.19% iron, 26.95% oxygen, 10.55% carbon, and 12.55% nitrogen.



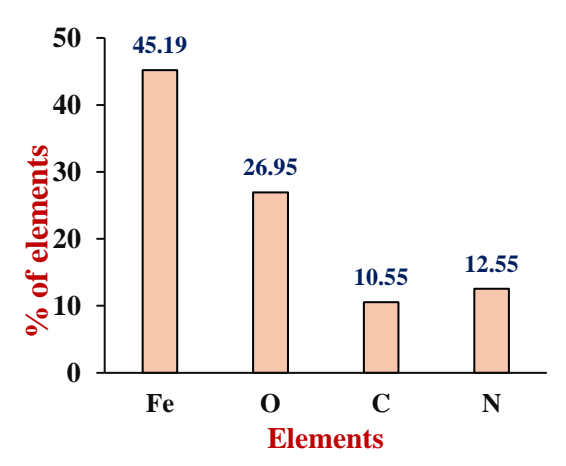


Figure 5.11: FE-SEM images, particle size distribution curve, and EDX report of PB@IONP.

5.3.3. Zeta-potential:

Zeta-potential of the nanoparticles was measured for 20 cycles. Based on the relative frequency, the zeta potential of PB@IONP is -21.39 mV, and the standard deviation is 1.32 mV. As the Prussian blue was coated on IONP, the zeta potential of the nanoparticles slightly decreased.

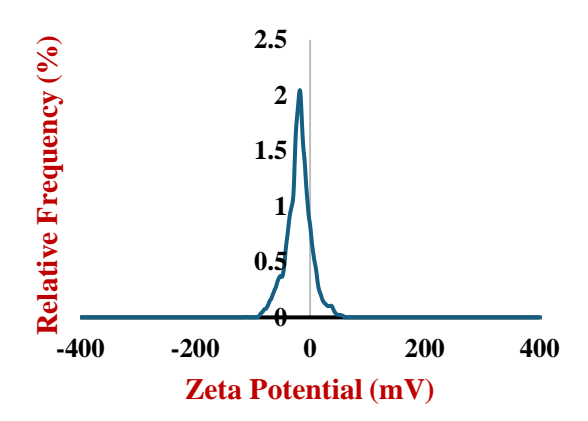


Figure 5.12: Zeta potential of PB@IONP in DI water.

5.3.4. XRD Analysis:

X-ray Diffraction (XRD) of PB@IONP was done at the Department of Metallurgy and Materials Science, IIT Indore. The angle of diffraction (2θ) was set as 20° to 80°. The XRD peak at 2θ of the nanoparticles was 17.5°, 24.7°, 35.5°, 35.69°, 40°,

 43.30° , 53.69° , 57° , 62.98° . It confirms the presence of IONP and Prussian blue ($2\Theta=17.5^{\circ}$, 24.7°) coating on it. After rigorous washing, some KCl salt was still present in the particles. The XRD peaks at 40° confirm the presence of KCl salt.

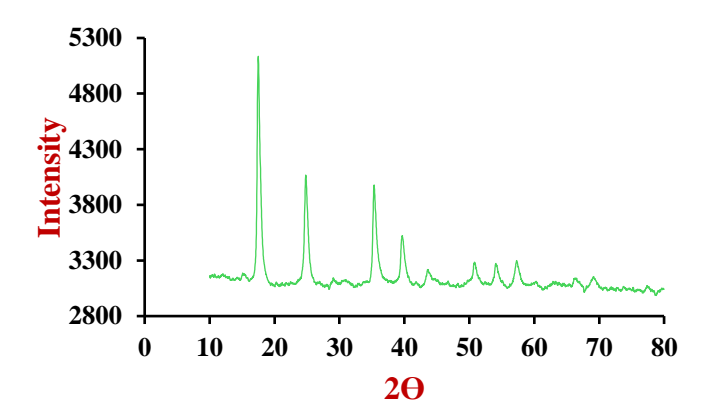


Figure 5.13: XRD peak of PBIONP at the corresponding 2θ peak.

5.4. Characterization of thin film:

5.4.1. Solubility in water:

The synthesized thin film was punched with the help of a paper punching machine to get a small, thin film. A small thin film was put in distilled water to check its water solubility and observe. After 5 minutes, the film is dissolved in water. Therefore, the Sodium alginate-based thin film is crosslinked with 1% (w/v) CaCl₂ to make it insoluble in water and increase the thin film's mechanical strength.²⁹

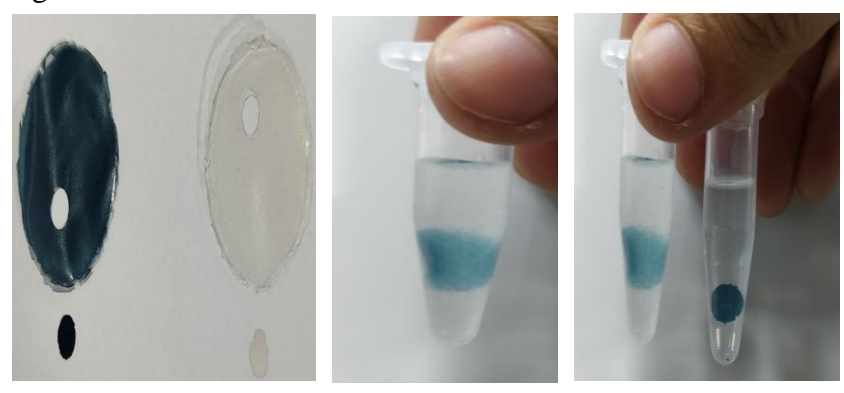


Figure 5.14: Observation of thin film's solubility in water and crosslinking step with 1% (w/v) CaCl₂.

5.4.2. FE-SEM images and EDX of thin films:

The FE-SEM of sodium alginate-drug-loaded, IONP, PBNP, and PB@IONP-loaded thin film has been observed, and the EDX report of all thin films confirms the elemental composition. The control, i.e., only drug-loaded SA thin film, has a smooth surface compared to the nanoparticles-drug-loaded SA thin film. The random distribution of the nanoparticles in the thin film makes it rough.

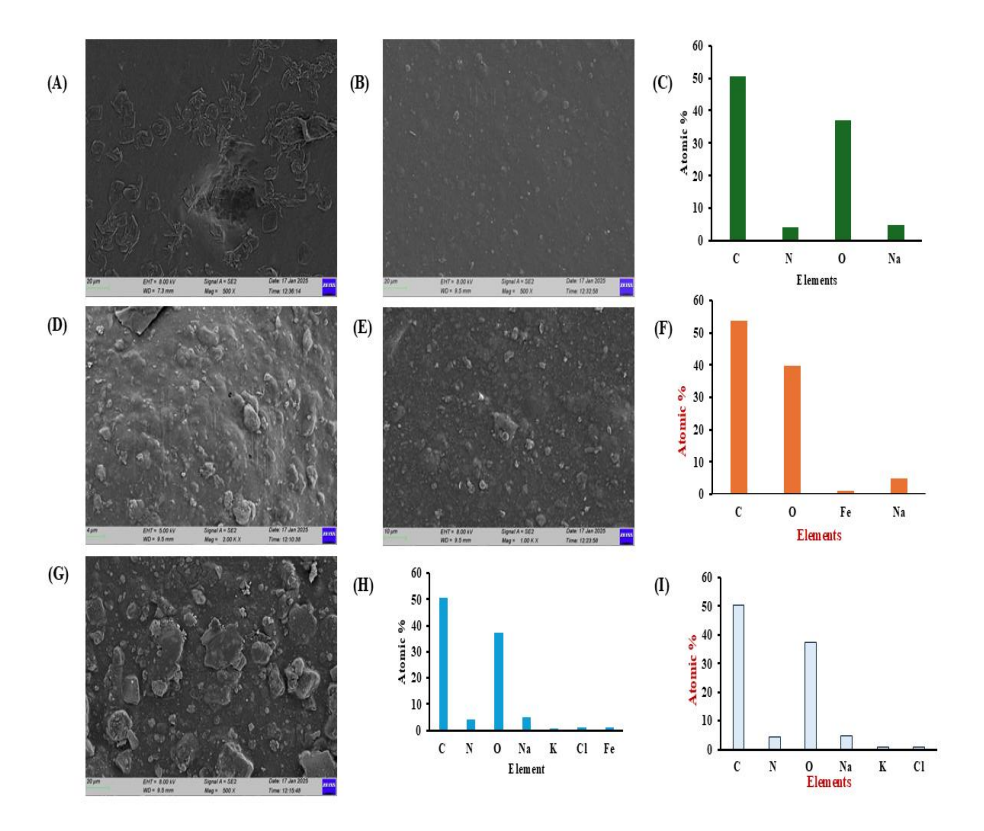


Figure 5.15: FE-SEM images and EDX of thin films: (A) SEM images of SA +D TF after CaCl₂ Crosslinking, (B) SEM of SA+D TF before crosslinking, (C) EDX of SA+D TF, (D) SEM of IONP TF, (E) SEM of PBNP TF, (F) EDX of IONP TF, (G) SEM of PB@IONP TF (H) EDX of PBNP TF (I) EDX of PB@IONP TF.

5.4.3. XRD analysis of Thin Films:

XRD of all four thin films was done, and the obtained data was plotted. This data confirmed the elemental composition of thin films. In case of SA+D TF, $2\theta = 16^{\circ}$ and 21° & drug: 34.5° , in IONP TF, $2\theta : 16^{\circ}$, 21° , 30.1° , 35.5° , 42.6° , 57.0° and 64.1° , in PBNP TF, $2\theta : 16^{\circ}$, 17.4° , 21° , 24.7° , 35.1° , 39.9° , 43.5° , 50.8° , 54.1° , 57.3° , 65.2° and 68.3° , and finally in PB@IONP TF, $2\theta : 19^{\circ}$, 22.5° , 35.5° , 38.1° , 50.8° , 61.7° , 62.6° and 73° . Here, in the case of PBNP & PB@IONP TF, 2θ at 39.9° , 50.8° , and 50.1° confirms the presence of potassium chloride salts.

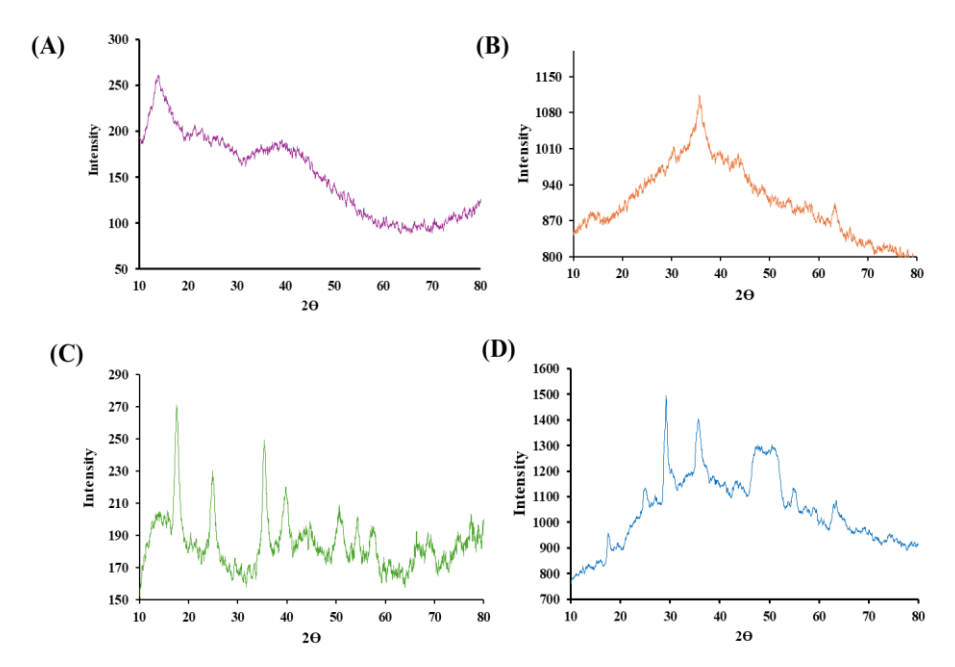


Figure 5.16: XRD images of thin films: (A) XRD peak of SA+D TF, (B) XRD peak of IONP TF, (C) XRD peak of PBNP TF, (D) XRD peak of PB@IONP TF.

5.4.4. AFM of thin films:

Atomic Force Microscopy (AFM) is a powerful technique used to analyze surfaces of thin films at the nanoscale. It measures the forces between a sharp probe (attached to a cantilever) and the sample surface. The deflection of the cantilever is detected using a laser beam, allowing the creation of high-resolution images of the surface. Our experiment was done in Non-Contact Mode. In Non-Contact Mode (NCM), the probe does not touch the sample surface. Instead, it oscillates near the

surface, detecting changes in forces such as van der Waals forces. This mode is beneficial for delicate samples, as it avoids physical contact that could damage the surface. ³⁰

AFM of all four thin films was done, and the 3D images, average roughness (Sa), grain size, and developed interfacial area ratio (SDR) are described. In SA+D TF, Sa: $0.0017~\mu m$, grain size: 6.1~nm, SDR: 0.015%; in IONP TF, Sa: $0.0033~\mu m$, grain size: 26.85~nm, SDR: 0.64%; in PBNP TF, Sa: $0.0044~\mu m$, grain size: 46.58~nm, SDR: 0.015%, and in PB@IONP TF, Sa: $0.0093~\mu m$, grain size: 49~nm, SDR: 0.469~%. A smooth surface in control SA+D TF and a rough surface in nanoparticles loaded thin film were observed through AFM.

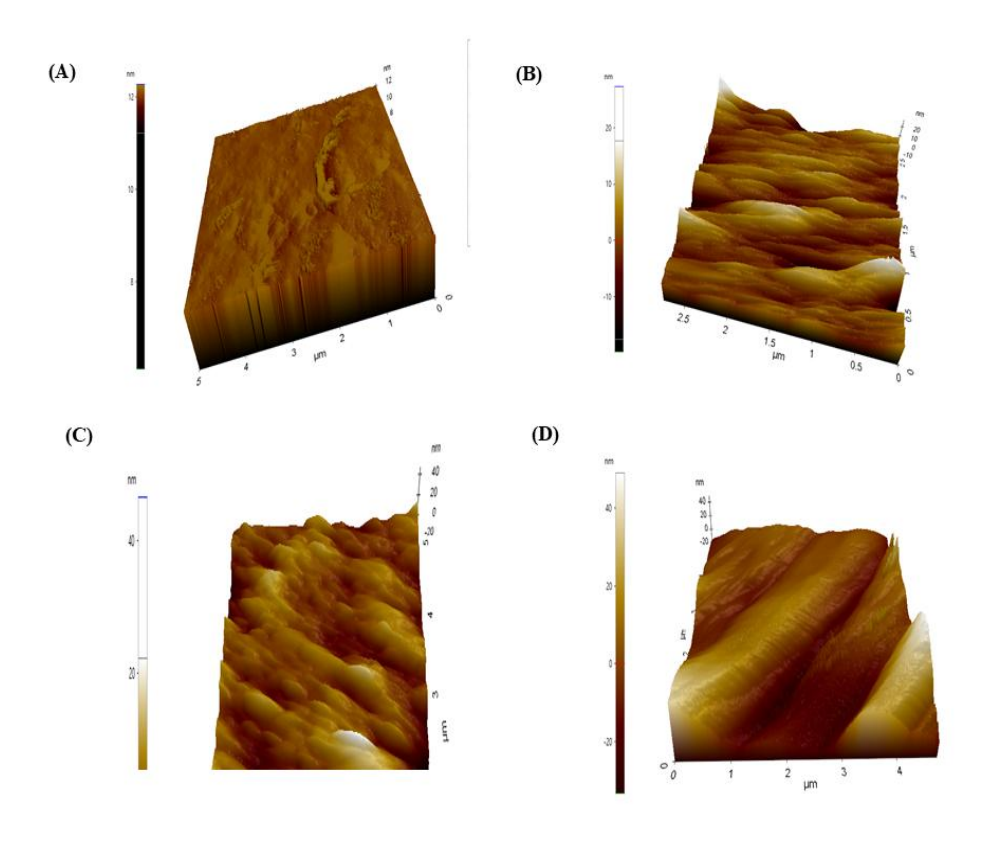


Figure 5.17: (A) AFM 3D images of SA+D TF, (B) AFM 3D images of IONP TF, (C) AFM 3D images of PBNP TF, (D) AFM 3D images of PB@IONP TF.

5.4.5. Swelling Index (SI) of thin films:

In the current research work, the swelling index was determined by measuring the weight of swelling of thin films in the given DI water. All the thin films exhibited very high values of swelling index. The results of the swelling index for all thin films are shown in the figure. The swelling index was higher in SA TF and PBNP TF compared to IONP and PBIONP TF. All the thin films exhibited a swelling index between 750 and 1050. The higher swelling index of SA TF and PBNP was due to free spaces and the presence of hygroscopic salts, respectively. However, the swelling index is also dependent on the degree of crosslinking. There was a slight change in the swelling index in the thin film due to different cross-linking degrees, though all were kept in the cross-linking solution simultaneously. A higher degree of cross-linking retards the swelling ability of the system and maintains the physical integrity of the thin films.²⁶

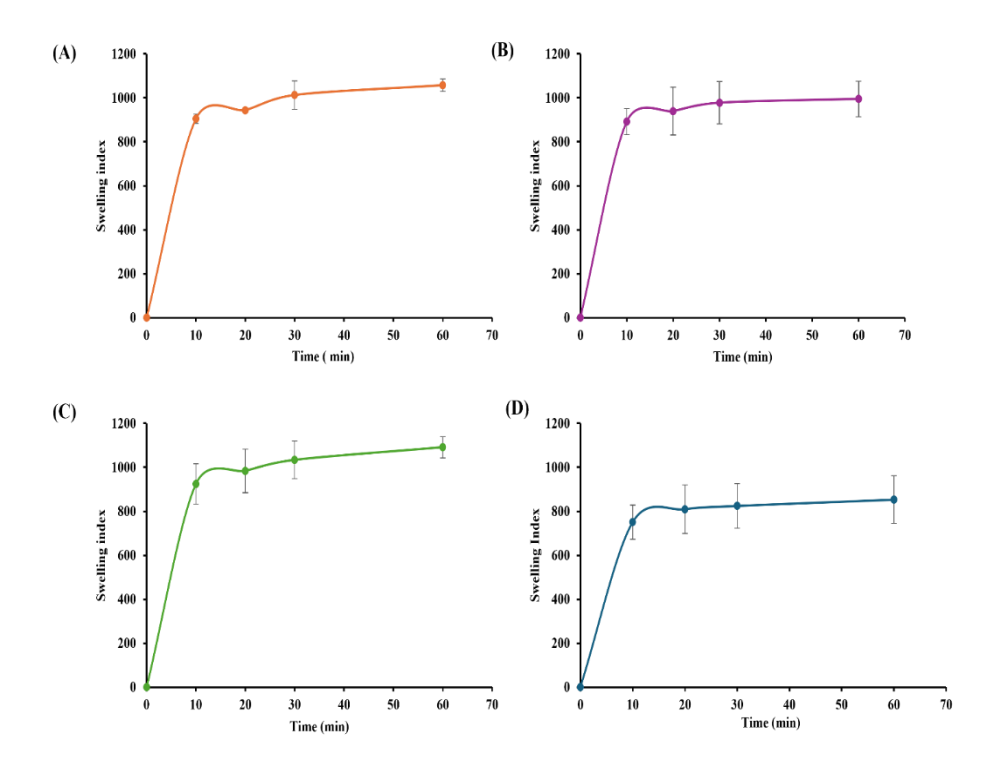


Figure 5.18: Swelling index of all 4 thin films immersed in 1 ml DI solution: (A) SI of SA+D TF, (B) SI of IONP TF, (C) SI of PBNP TF, (D) SI of PB@IONP TF.

5.5. Photo-thermal efficiency of nanoparticles:

The photo-thermal efficiency of the three nanoparticles was successfully measured by exposing them to 808 nm, 1 W NIR-laser. Two concentrations of the three nanoparticles were taken: 5 mg/ml and 500 μ l/ml.

A good temperature rise was observed when the IONP, PBNP, and PB@IONP were exposed to an NIR laser (1W, 808 nm) at varying times (0, 2.5, 5, 10 mins) and a constant pulse of 1 W. For a 5 mg/ml concentration, in the case of IONP, the maximum temperature rise was around 25.3°C; in the PBNP, the maximum temperature rise was around 25.6°C, and PB@IONP showed a maximum of 27.45°C when exposed for 10 min. For a 500 μl/ml concentration, the IONP TF has shown 15.6°C, the PBNP TF has shown 19.9°C, and the PB@IONP has shown 23.85°C after 10 minutes of laser exposure. The comparative study depicted and confirmed the possibility of a massive temperature rise in PBNP and PB@IONP compared to IONP.

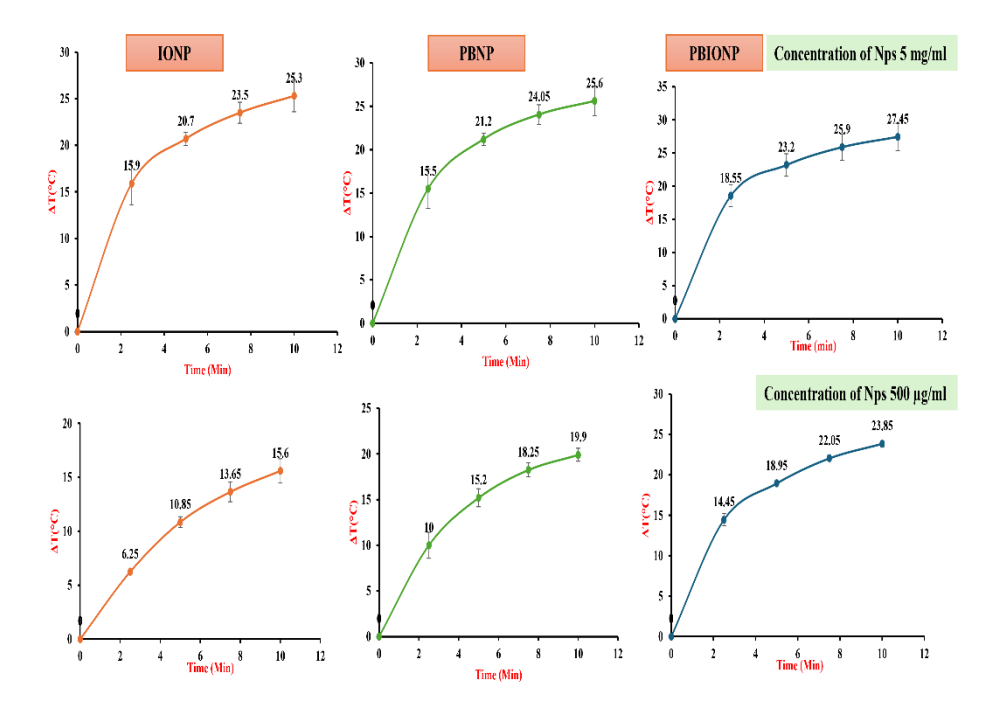


Figure 5.19: The graph of temperature rise in IONP, PBNP, and PB@IONP under 808 nm NIRlaser in varying time & constant pulse, and their comparative analysis has been plotted.

5.6. Photothermal efficiency of thin film:

The photothermal efficiency of IONP, PBNP & PB@IONP-loaded sodium alginate thin film was tested for photothermal efficiency under NIR-laser 1 W, 808 nm. It was done in two different volumes of DI solution: 1 ml and 200 μ l.

When IONP, PBNP & PB@IONP-loaded thin film were exposed to a NIR laser (1W, 808 nm), a suitable temperature was observed. In 1 ml DI solution, in the case of IONP-loaded thin film, the maximum temperature rise has shown 17.35°C; in PBNP-loaded thin film, the maximum temperature has risen to 17.35°C, and the PB@IONP has shown a maximum temperature up to 19.75°C. But in 200 µl DI solution in a 96-well plate, IONP TF has shown 20.7°C, PBNP TF has shown 23.05°C, and PB@IONP TF has shown 24.4°C. In the case of our control, SA+ D TF has shown a maximum 2-5° C temperature rise. The Comparative study depicted and confirmed the possibility of a massive temperature rise in PBNP and PB@IONP-loaded thin film compared to IONP thin film.

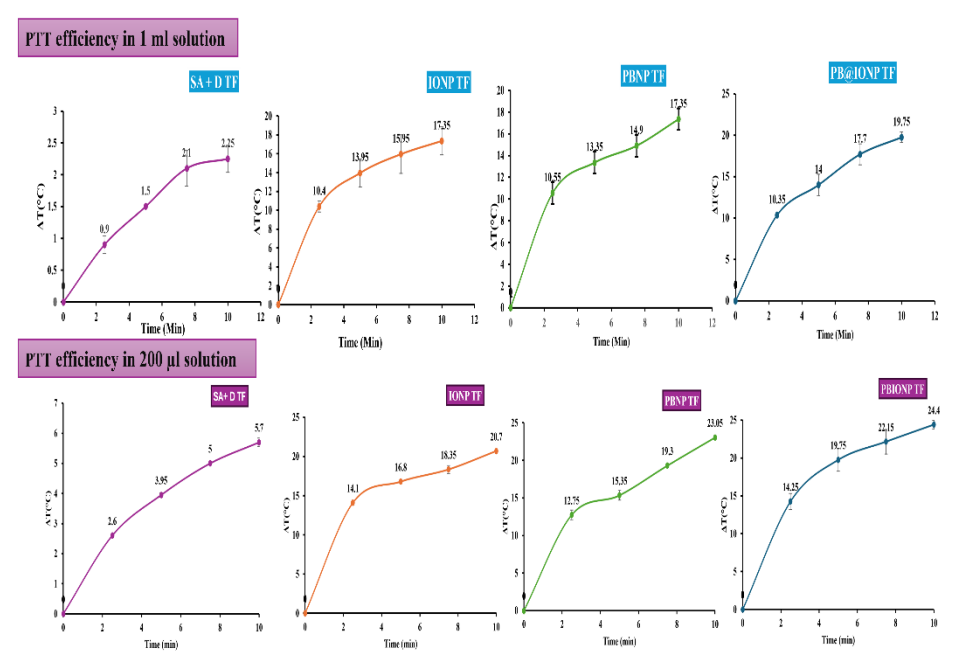


Figure 5.20: Graphical representation of temperature rise in IONP, PBNP & PB@IONP-loaded thin films in 1 ml and 200µl solution after exposure with 808 nm NIR laser for different time intervals (2.5, 5, 7.5, and 10 mins) and constant pulse (1W, 808 nm).

5.6.1. IR-thermal Imaging:

IR thermal imaging was performed to determine the heat emitted from various NIR-responsive materials. The thermal energy released from the material, in the form of infrared (IR), is captured by a thermal imaging camera and visualized as a thermogram, the visual output created by the thermal camera. The thermograph has different colors of the visible range (400 to 700 nm), demonstrating different temperatures. The high-temperature areas are represented by red color, whereas the low-temperature areas are represented by blue. This is the basic principle of the IR-thermal camera.

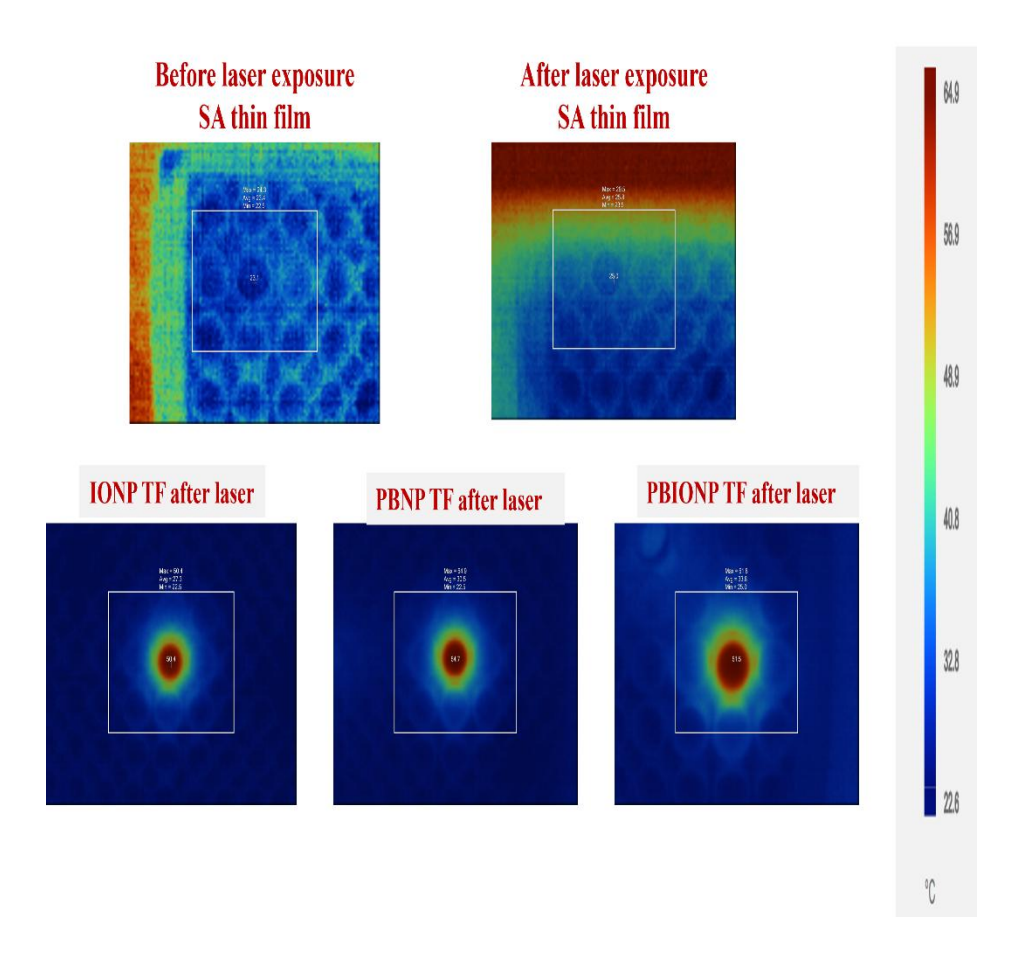


Figure 5.21: Thermal image of all four thin films by the exposure to NIR 1 W, 808 nm laser for 5 minutes by using an IR thermal imaging camera.

After exposure to NIR 1 W, 808 nm laser on the thin films kept in a 96-well plate containing 200 μ l DI, the temperature rise was recorded by the

thermal camera as shown in Figure 23. The maximum temperature recorded was 64.7°C in PBNP TF and 61.5°C in PBIONP TF to control SA TF. Also, the IONP TF showed a temperature rise to 50.4°C. This indicates that while exposing a 1 W, 808 nm laser for 5 minutes, the temperature of the thin films and surroundings increased, indicating the characteristics of the photothermal effect.

5.7. Characterization of 5-fluorouracil (5-FU):

5.7.1. Absorbance spectrum of 5-FU:

The UV-visible spectrophotometric absorbance of 5-FU dissolved in distilled water was observed at a maximum peak of 266 nm. The previously published data showed similar absorbance.³¹

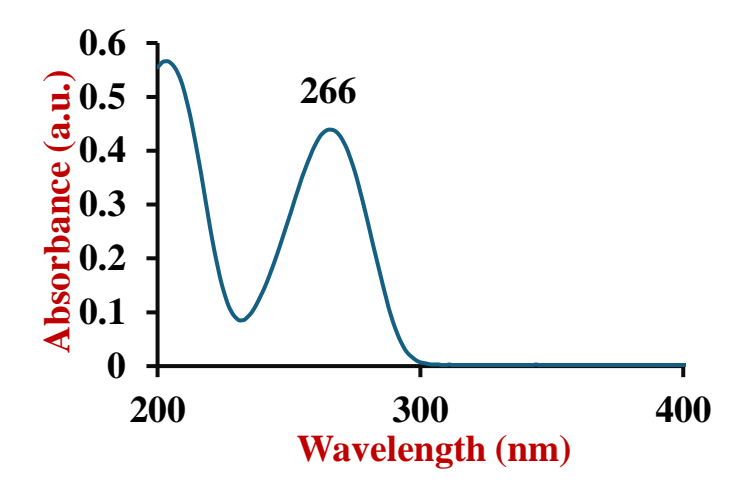
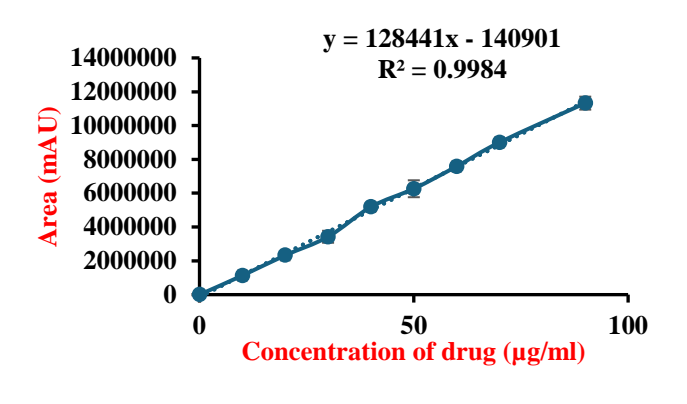


Figure 5.22: The maximum absorbance peak of 5-FU at 266 nm.

5.7.2. Calibration Curve of 5-FU:

The calibration curve of 5-FU was plotted using the chromatographic area of samples having different diluted concentrations at 266 nm in HPLC. The retention time of the drug was 7.5 minutes. The calibration curve has a regression coefficient R^2 value of 0.998. The equation of the curve is y=128441x-140901. The equation was further used to calculate the drug loading efficiency and drug release kinetics from the thin film.



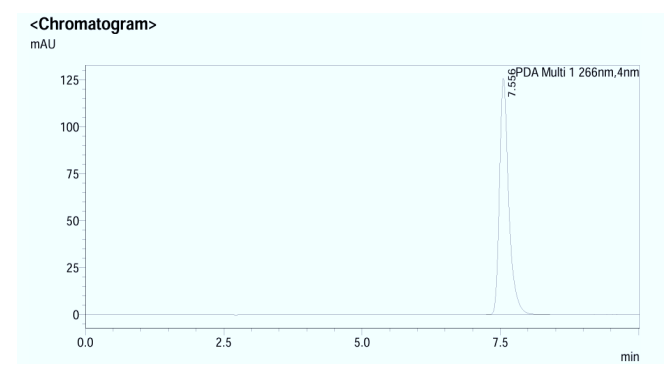


Figure 5.23: Standard curve and retention time of 5-FU analyzed by HPLC.

5.8. Drug-Encapsulation Efficiency:

Drug encapsulation efficiency is most vital part of any drug delivery experimentation. It is essential to determine the drug release kinetics of the material i.e. the thin film. During solution making, how much drug is incorporated inside the thin film, that is the drug encapsulation efficiency of thin films. Here, the drug may be present in the surface of the thin film or on the inside of the thin film. As the thin films contain surface-associated drugs, the drug was released during crosslinking with the CaCl₂ solution. So, after the crosslinking process, we checked the final drug encapsulation efficiency of each thin film. After the crosslinking process, the drug encapsulation efficiency of SA+D thin film is 58.14%, IONP TF is 56.06%, PBNP TF is 58.73%, and PB@IONP TF is 57.47%. This was useful for further calculation of drug kinetic release studies.

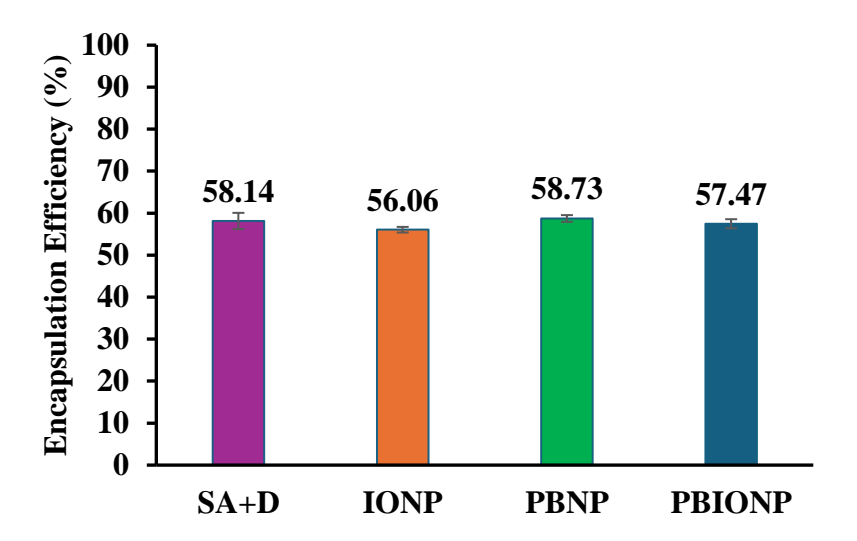


Figure 5.24- Drug release percentage from thin films after CaCl₂ treatment and final drug encapsulation efficiency of each thin film.

5.9. In Vitro Drug Release Profiles in Thin Film:

IONP, PBNP, and PB@IONP-loaded thin films were extensively studied for drug release profiles. In laser-induced drug release, the absorbance of the 1 mL solution was measured in a spectrophotometer. Without the laser drug release method, the absorbance of 1 ml of a 10 ml solution was measured in a spectrophotometer. Without laser exposure, the drug release percentage was calculated using the calibration equation obtained through a standard HPLC chromatogram. The cumulative drug release percentage of our control drug-loaded sodium alginate (SA+D) was observed at 50% after 5 hrs. The IONP-loaded thin film showed cumulative drug release at 70% after 10 hrs. The PBNP-loaded thin film has shown cumulative drug release at 70% after 10 hrs. The PB@IONP thin film has shown cumulative drug release at 80% after 24 hrs. In the case of laser-induced drug release studies, the SA+D TF has demonstrated 43 % drug release after 10 minutes of laser exposure, the IONP TF has shown 65% drug release after 10 minutes of laser exposure, the PBNP TF has shown 70 % drug release after 10 minutes, and the PB@IONP TF has demonstrated 81% drug release after 10 minutes of laser exposure. Therefore, sustained drug release was seen without laser

drug release, whereas burst drug release was seen under NIR-laser exposure to thin film.

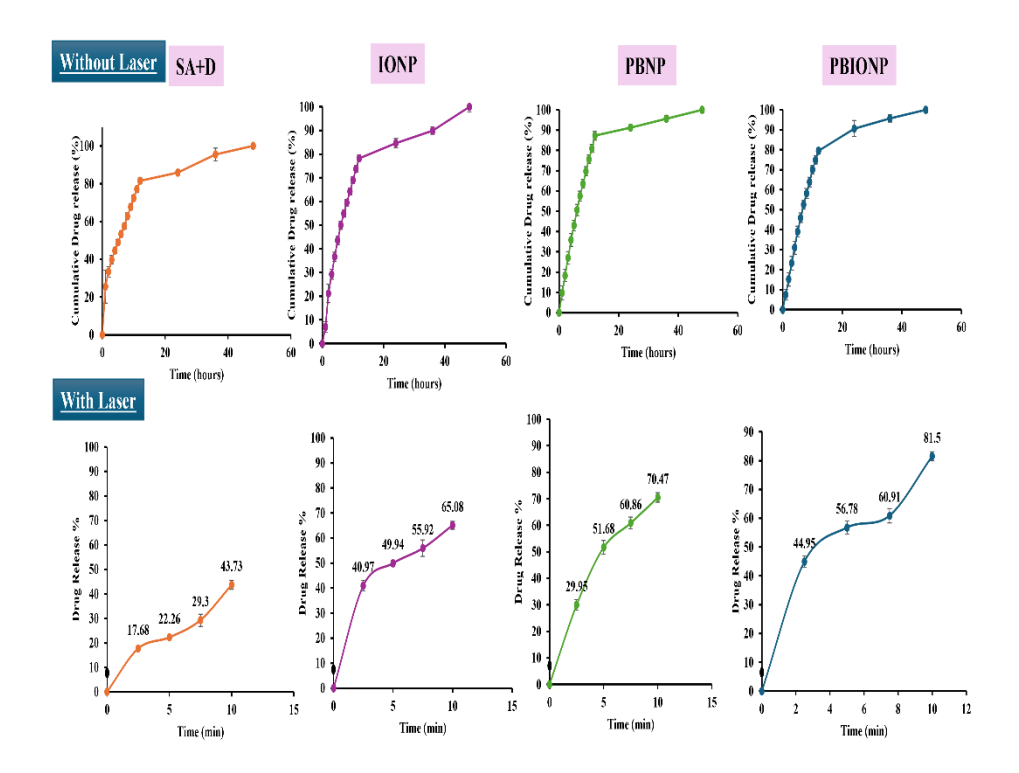


Figure 5.25: The drug release percentage from SA+D, IONP, PBNP, and PB@IONP-loaded thin films without laser exposure (upper) and with laser exposure (lower).

5.9. Nanoparticles release profile:

We simultaneously analyzed the nanoparticle's release profile during the drug release studies, which is crucial for photothermal therapy. In the case without laser, no nanoparticles were released for up to 1 hr, but very slowly, nanoparticles were released after 6 hr, up to 48 hrs. On the other hand, under NIR-laser irradiation for 10 minutes, gradual nanoparticle release was observed. Therefore, it is effective in photothermal killing of cancer cells under the laser irradiation. However, in the IONP thin film, no nanoparticle release was seen. Therefore, after carefull consideration, we kept IONP thin film aside and furthur forwarded With PBIONP and PBNP thin film.

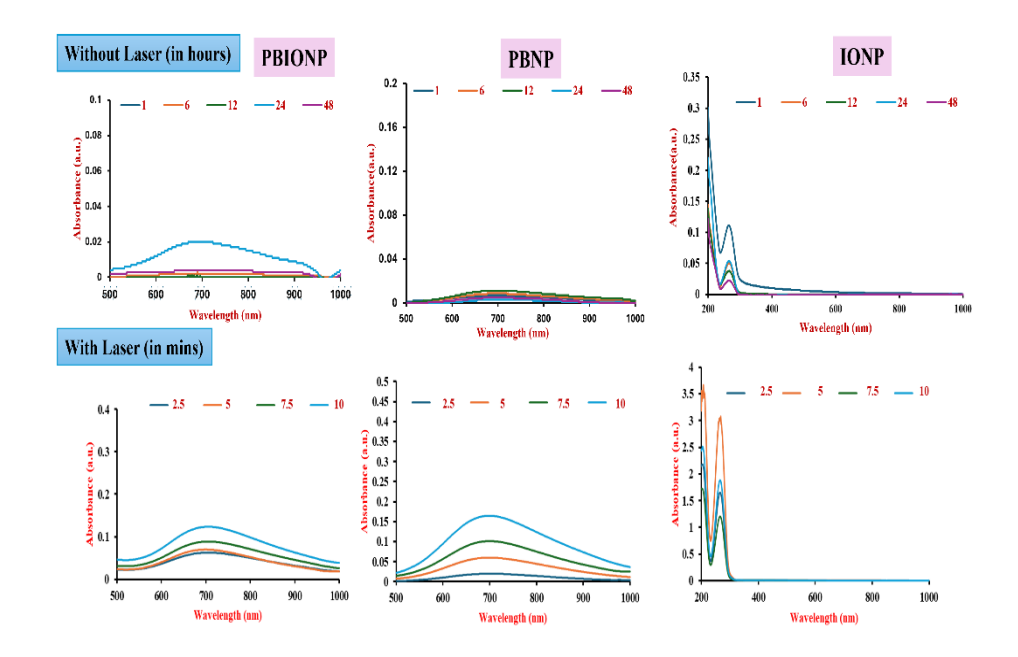


Figure 5.26: The NPs release profile from IONP, PBNP, and PB@IONP-loaded thin films without NIR-laser for different time intervals (1, 6, 12, 24, 48 hrs) and with 808 nm, 1 W NIR-laser exposure for different time intervals (2.5, 5, 7.5, and 10 mins).

5.11. In Vitro cytotoxicity of nanoparticles and drug by MTT analysis:

The cytotoxicity effect of nanoparticles was determined by performing a colorimetric MTT assay. This assay is based on the ability of viable cells to reduce soluble yellow MTT (3-(4,5-dimethylthiazol-2-yl)-2,5 2,5-diphenyltetrazolium bromide) to insoluble purple formazan crystals by NADPH-dependent oxidoreductase enzyme. Then, these insoluble crystals are dissolved using DMSO, and the resulting solution is quantified by taking absorbance at 570 nm and 590 nm using a spectrophotometric plate-reader.

Biocompatibility and cytotoxicity of synthesized nanoparticles, i.e., PBIONP and PBNP, are tested for their cytotoxicity in HEK-293. In all cases, the nanoparticles up to $400 \mu g/ml$ are safe for cells, describing their biocompatibility and non-cytotoxicity.

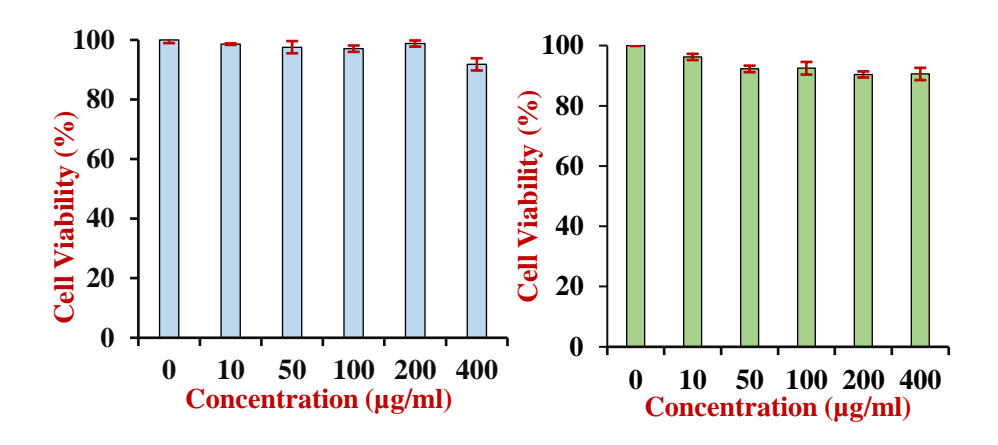


Figure 5.27- MTT assay of PBNP & PBIONP nanoparticles in HEK 293 cell line.

In this context, we have performed an *in vitro* cytotoxicity assay in MCF-7 and the desired oral cancer SCC-9 cell lines using the Alamar blue assay of PBIONP nanoparticles and determined the IC $_{50}$ of the drug. From the cell viability graph of drug-treated MCF-7 and SCC-9, the IC $_{50}$ of 5-FU is 43.49 μ M in the MCF-7 cell line and 4.5 μ M in the SCC-9. It shows a higher efficiency in oral cancer SCC-9 cell lines compared to MCF-7 cell lines. In case of PBIONP-treated MCF-7 and SCC-9, the IC $_{50}$ of 850 and 950 μ M concentrations of PBIONP have been shown to MCF-7 and SCC-9 cell lines, respectively. So our synthesized PBIONP is biocompatible and non-cytotoxic.

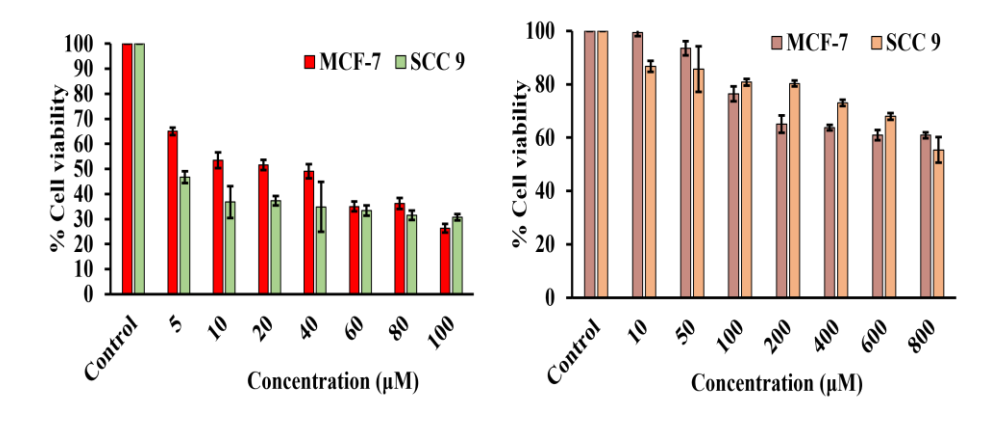
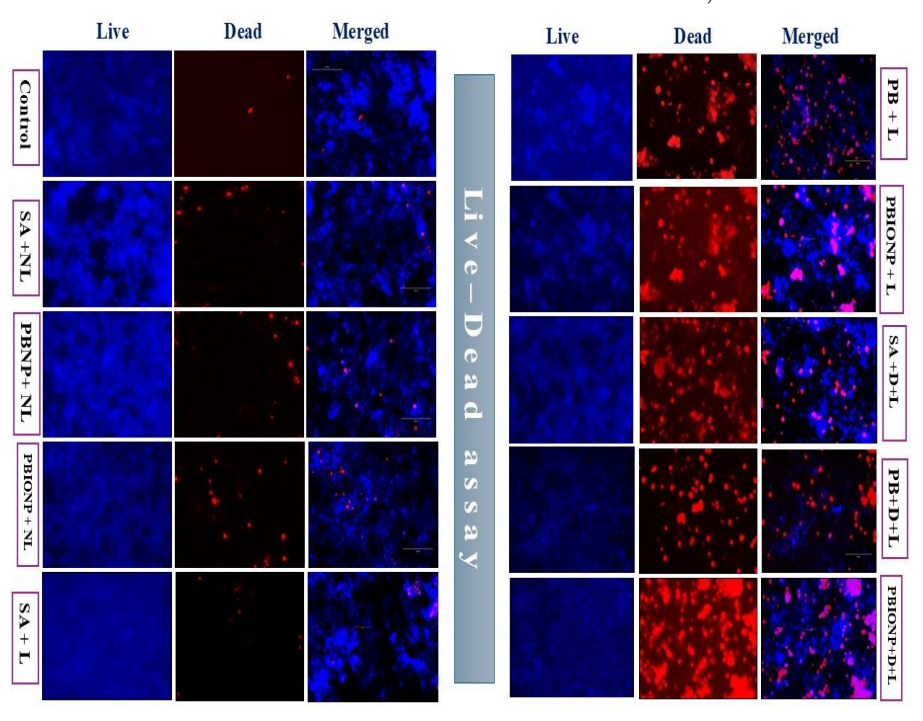


Figure 5.28- *In vitro* cytotoxicity assay of 5-Fluorouracil (left) and PB@IONP (right) nanoparticles in breast cancer cell line MCF-7 and oral cancer SCC-9 using Alamar blue assay.

5.12. Live-dead assay using chemo-photothermal therapy:

For the live-dead cell analysis, the MCF-7 cells were treated with thin films followed by laser exposure. After laser exposure and a timedependent incubation period, the cells were stained with GFAFC and PI for live and dead cells, respectively. The GF-AFC stain penetrates the live cells, and the cellular aminopeptidase enzyme removes the glycine and phenylalanine acid residues and releases blue, fluorescent AFC. The blue intensity is directly proportional to the number of viable cells. On the other hand, PI-stained dead cells in red. It cannot pass through live intact cell membranes but can freely enter the membrane-compromised cell, intercalate into dsDNA, and emit red fluorescence. In various combinations, MCF-7 cells were treated with one thin film of each, i.e., SA +D, PBNP, and PBIONP TF. The cells with thin film were exposed 1W, 808 nm laser for 5 minutes, followed by incubation for 6 hours. The live-dead cells were visualized with fluorescence microscopy. The maximum cell death was seen in cells incubated with PBIONP & PBNP TF for 6 hours (75-90%) because of a maximum temperature rise and high drug release kinetics. This shows that the synthesized PBNP and PBIONP TF have excellent photothermal properties and chemophotothermal effects in killing cancer cells effectively. Therefore, cell death occurred when we treated MCF-7 with laser 1 W, 808 nm.



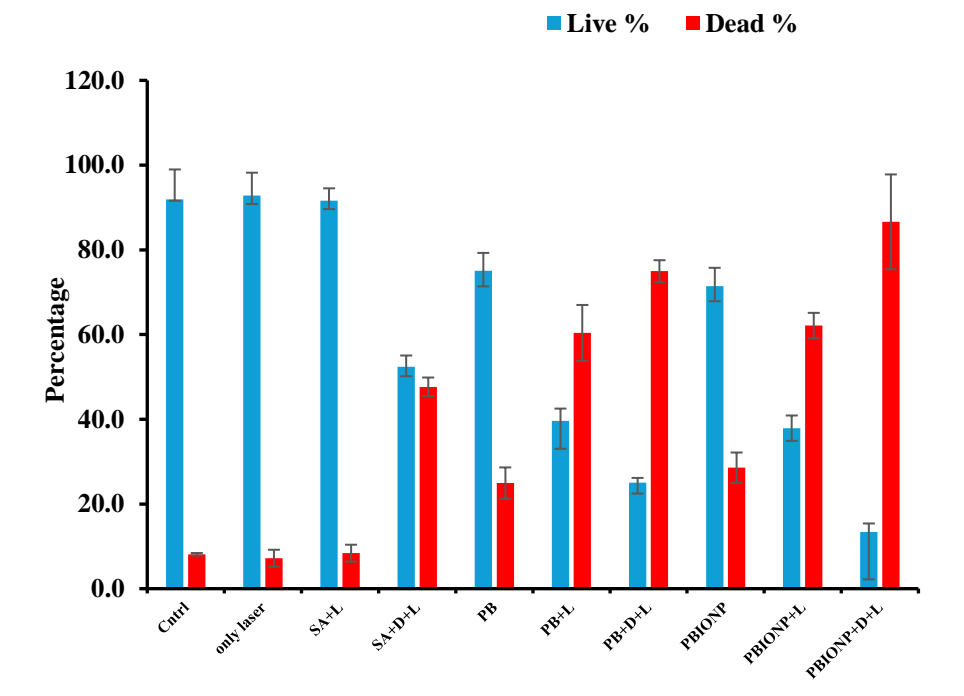


Figure 5.29: Live and Dead analysis- Fluorescence image of live and dead analysis by fluorescent microscopy by treating MCF-7 cells with different combinations of thin films, followed by exposure to a 1 W, 808 nm NIR laser, with a graphical representation of the percentage of live and dead cells.

Next, the MCF-7 cells were treated with most potential multiple PBIONP thin films for up to 5 thin films. The cells were exposed to 1 W, 808 nm NIR laser for 10 minutes, followed by a 12-hour incubation for sustained drug release. When we expose nanoparticles with a laser, there is a burst release of the drug, due to which cell death occurs. The cells treated with multi-PBIONP TFs showed more cell death than the control and single thin film, especially 4 & 5 TFs, which showed maximum cell death. The increasing red color intensity graph proves the effective chemo-photothermal effect on cells, leading to high death occurrence. This implies that cell death occurs due to the photothermal effect and laser-induced drug release.

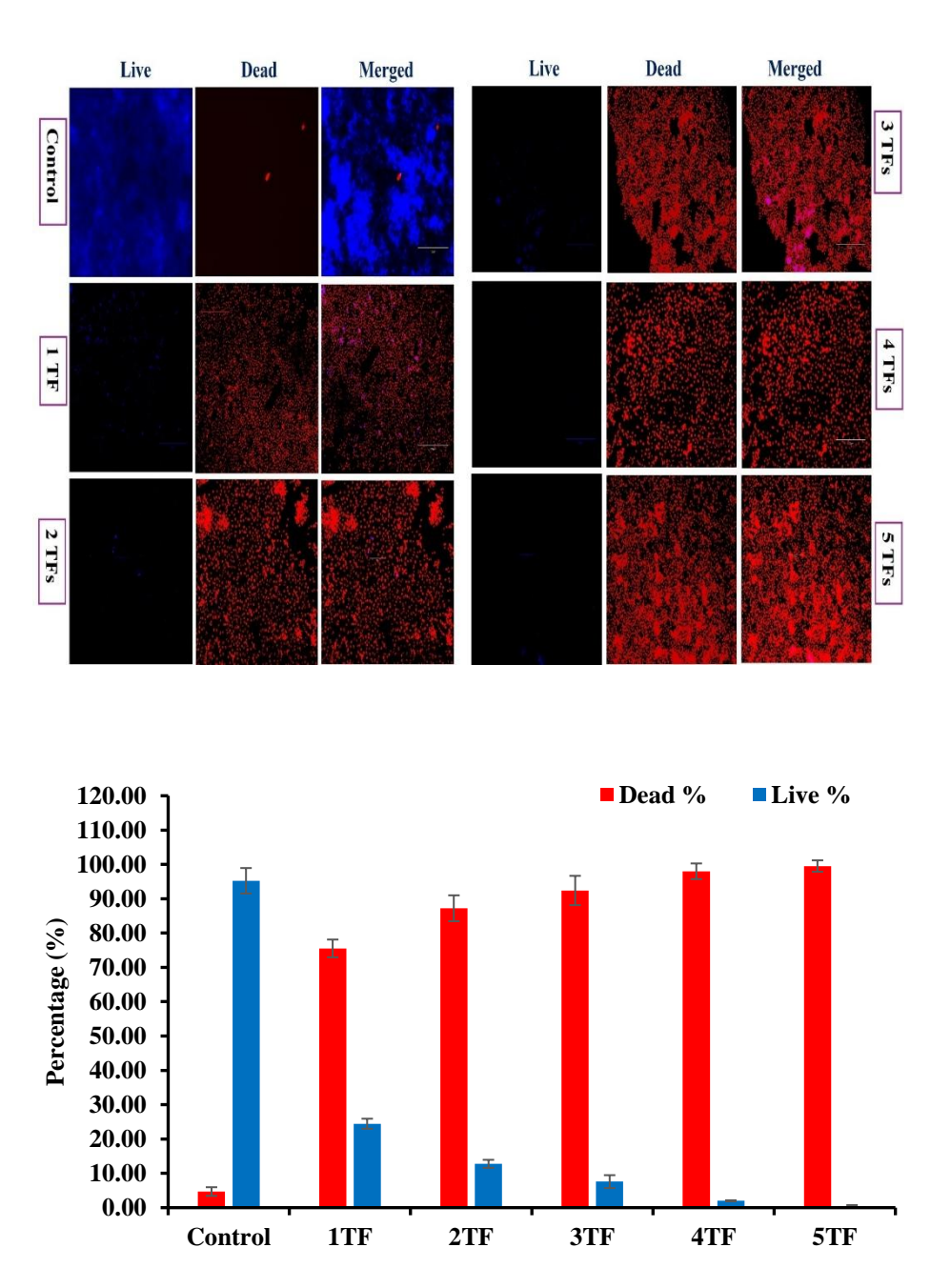
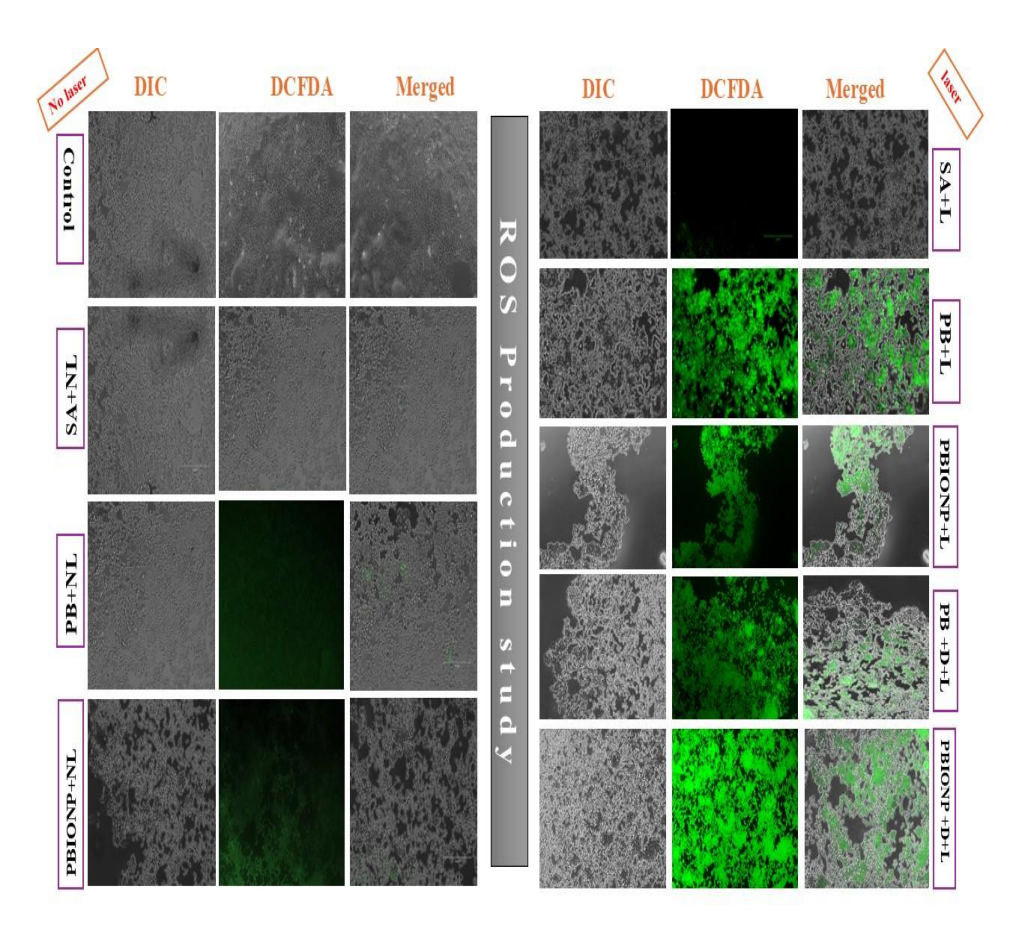


Figure 5.30: Live and Dead analysis using multiple PBIONP TF in MCF-7 cells exposed to laser and a long incubation period (12 hours) for chemo-photothermal therapy, and the graphical representation of the percentage of live and dead cells.

5.13. ROS study in cells:

MCF-7 cells were treated with different combinations of three, i.e., SA, PBNP, and PBIONP TF, focusing on drug and laser exposure. The treated cells were incubated for 6 hours. For Reactive Oxygen Species (ROS) production studies in MCF-7 cells, dichlorodihydrofluorescein diacetate (DCFDA) stain was used. DCFDA is a non-fluorescent, cell-permeable stain that is converted to dichlorofluorescein. During the laser exposure and incubation period, the increasing temperature and the released drug 5-FU generate ROS inside the cell, and the ROS oxidize the dichlorofluorescein to highly green fluorescent dichlorofluorescein. The ROS-producing cells were visualized using fluorescence microscopy. The maximum ROS production was seen in drug-loaded PBIONP thin film (22-fold ROS generation change) and drug-loaded PBNP TF (18-fold ROS generation change) with laser-treated cells compared to the control and SA TF. The fold ROS generation change graph for various combinations is plotted for better understanding.



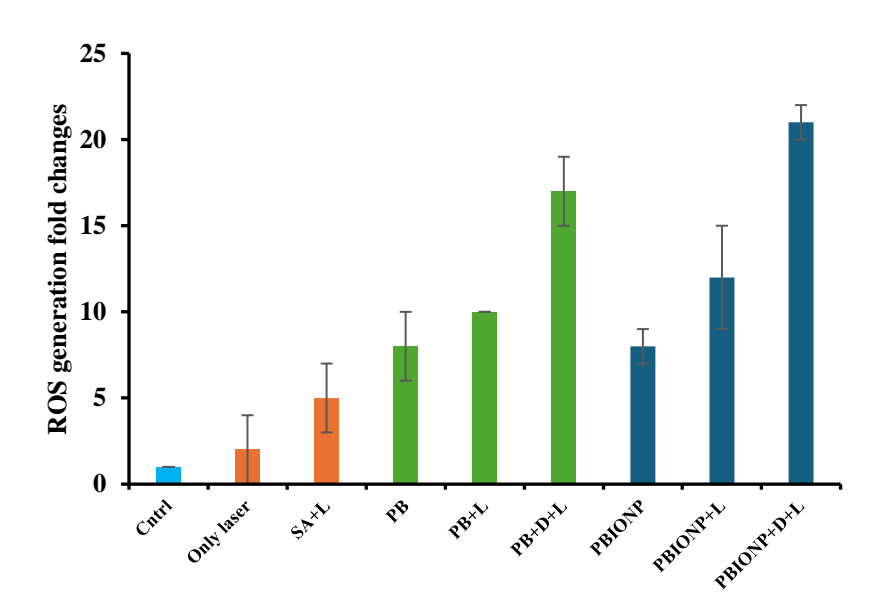


Figure 5.31: ROS production studies in cells treated with thin films under laser exposure and drug release conditions. The DCFDA color, i.e., ROS generation fold change graph was calculated.

5.14. Apoptosis study on cells:

MCF-7 cells were treated with different combinations of three, i.e., SA, PBNP, and PBIONP TF, focusing on drug and laser exposure. The treated cells were incubated for 6 hours. For apoptosis studies in MCF-7 cells, annexin V stain was used. Annexin V is a protein with a high affinity for phosphatidylserine (PS). In the normal cell, the PS is located inside, the stain can't bind, but in the apoptotic cell, the PS is exposed in the outer membrane, and annexin V binds with PS, providing green fluorescence. PI stain was used for late-stage apoptosis or necrosis and dead cell determination. Apoptosis is one of the key highly regulated mechanisms of cell death. Amongst physiological processes, apoptosis is a well-characterized, controlled morphological characteristic of cell death. The vital hallmark and earliest feature of the apoptotic process is the exposure of PS on the plasma membrane. During the laser exposure and incubation periods, the increasing temperature and drug release lead to the exposure of PS on the outer membrane. In this study, the maximum

apoptosis (intensity is 35) was seen in drug-loaded PBIONP TF treated cells. The annexin V colour intensity graph was plotted to understand the degree of apoptosis in treated MCF-7 cells.

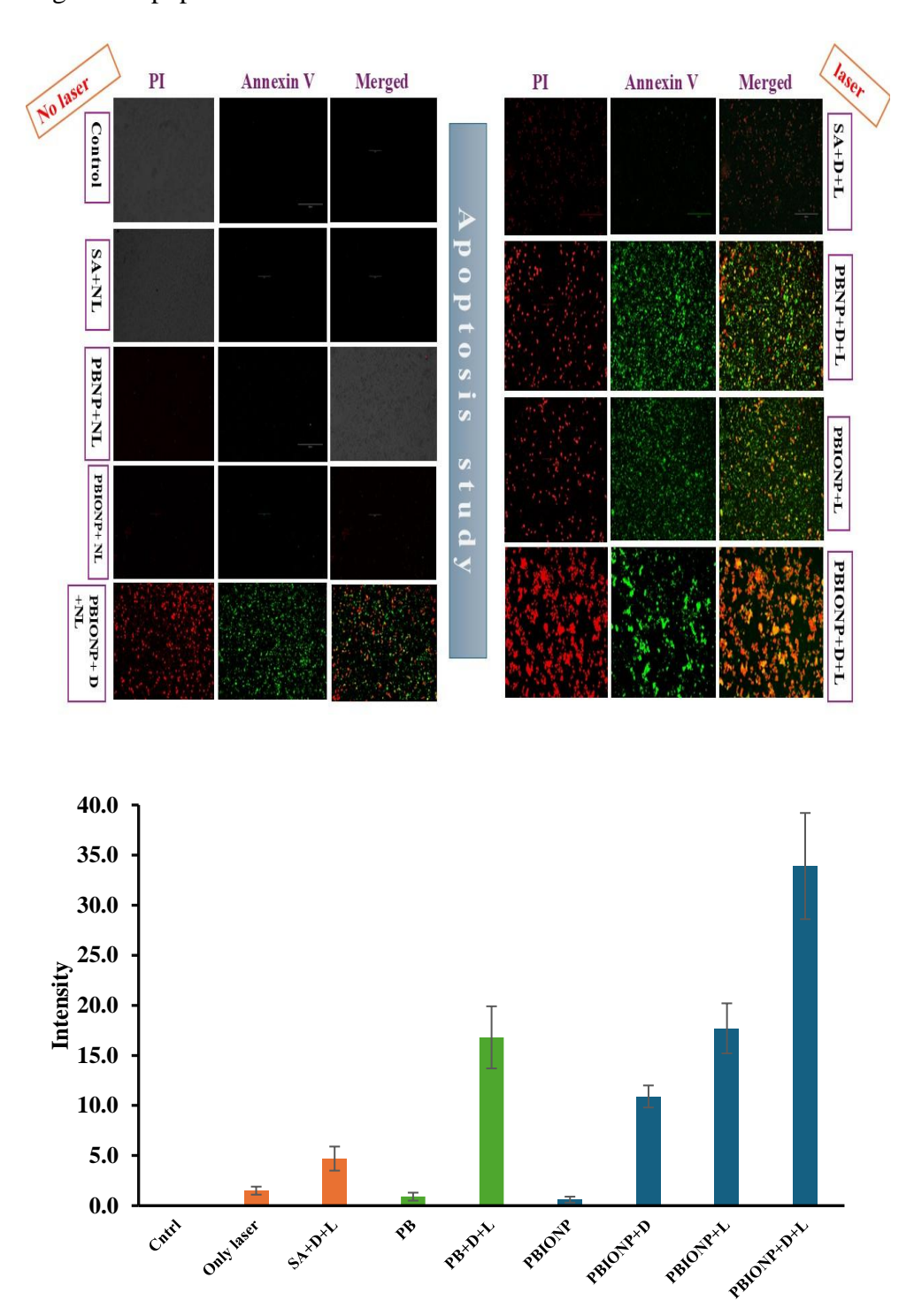


Figure 5.32: Apoptosis studies in cells treated with thin films under laser exposure and drug release conditions. The Annexin V color intensity graph was calculated.

Chapter 6

Conclusions

This research project presents the successful development and comprehensive evaluation of an NIR-responsive thin film platform for chemo-photothermal therapy in breast cancer treatment. The research demonstrates the synthesis and characterization of iron oxide nanoparticles (IONPs), Prussian blue nanoparticles (PBNPs), and Prussian blue-coated iron oxide nanoparticles (PB@IONPs), each exhibiting distinct photothermal properties and biocompatibility. Incorporating these nanoparticles, along with the chemotherapeutic agent 5-fluorouracil (5-FU), into sodium alginate-based thin films enabled the creation of a multifunctional system capable of both sustained and laser-triggered drug release. The PB@IONP-loaded thin films, in particular, showed superior photothermal conversion efficiency and drug release kinetics, achieving up to 81.5% drug release within 10 minutes of NIR laser exposure and 80% over 24 hours in the absence of laser, indicating their potential for precise, on-demand therapy. In vitro cytotoxicity assays confirmed the biocompatibility of the nanoparticles and the efficacy of the thin films in inducing significant cancer cell death when combined with NIR irradiation, highlighting the synergistic effect of chemo-photothermal therapy. The system also facilitated efficient generation of reactive oxygen species (ROS) and promoted apoptosis in cancer cells, further validating its therapeutic potential.

These findings align with recent advances in nanomaterials-based chemophotothermal therapy, emphasizing the advantages of combining localized hyperthermia with controlled drug delivery to enhance therapeutic outcomes, minimize systemic toxicity, and overcome limitations associated with conventional cancer treatments. The dual-action approach of the developed thin films, leveraging both photothermal ablation and chemotherapeutic delivery, addresses critical challenges in breast cancer therapy, such as drug resistance, non-specific toxicity, and inadequate drug release profiles. Moreover, the platform's ability to provide minimally invasive, tunable, and targeted treatment offers significant promise for clinical translation. The modularity of the thin film system allows for adaptation to other drug molecules and cancer types, potentially broadening its impact within the field of oncology. Future research should focus on *in vivo* validation, long-term safety assessment, and optimization for large-scale manufacturing and clinical application.

Overall, the developed NIR-responsive thin film system represents a promising advancement in the field of targeted breast cancer treatment. By leveraging the dual-action of photothermal ablation and chemotherapeutic drug release, this approach offers a minimally invasive, tunable, and effective strategy for combating aggressive and drug-resistant cancer types. Future work should focus on *in vivo* validation and optimization of the system for clinical translation, aiming to improve patient outcomes and expand the therapeutic possibilities beyond breast cancer and potentially other solid tumors.

References

- (1) Global cancer burden growing, amidst mounting need for services. https://www.who.int/news/item/01-02-2024-global-cancer-burden-growing--amidst-mounting-need-for-services (accessed 2025-05-03).
- (3) Godet, I.; M. Gilkes, D. BRCA1 and BRCA2 Mutations and Treatment Strategies for Breast Cancer. *Integr Cancer Sci Ther* **2017**, *4* (1). https://doi.org/10.15761/ICST.1000228.
- (4) Rébé, C.; Ghiringhelli, F. Cytotoxic Effects of Chemotherapy on Cancer and Immune Cells: How Can It Be Modulated to Generate Novel Therapeutic Strategies? *Future Oncology* **2015**, *11* (19), 2645–2654. https://doi.org/10.2217/FON.15.198.
- (5) Kaur, R.; Bhardwaj, A.; Gupta, S. Cancer Treatment Therapies: Traditional to Modern Approaches to Combat Cancers. *Molecular Biology Reports* 2023 50:11 **2023**, 50 (11), 9663–9676. https://doi.org/10.1007/S11033-023-08809-3.
- (6) Oudjedi, F.; Kirk, A. G. Near-Infrared Nanoparticle-Mediated Photothermal Cancer Therapy: A Comprehensive Review of Advances in Monitoring and Controlling Thermal Effects for Effective Cancer Treatment. *Nano Select* **2025**, *6* (3), e202400107. https://doi.org/10.1002/NANO.202400107.
- (7) Kou, X.; Zhao, Q.; Xu, W.; Xiao, Z.; Niu, Y.; Wang, K. Biodegradable Materials as Nanocarriers for Drugs and Nutrients. *J Renew Mater* **2020**, *9* (7), 1189–1211. https://doi.org/10.32604/JRM.2021.015268.
- (8) Kadkhoda, J.; Tarighatnia, A.; Barar, J.; Aghanejad, A.; Davaran, S. Recent Advances and Trends in Nanoparticles Based Photothermal and Photodynamic Therapy. *Photodiagnosis Photodyn Ther* **2022**, *37*, 102697. https://doi.org/10.1016/J.PDPDT.2021.102697.

- (9) Baalousha, M. Aggregation and Disaggregation of Iron Oxide Nanoparticles: Influence of Particle Concentration, PH and Natural Organic Matter. *Science of The Total Environment* **2009**, *407* (6), 2093–2101. https://doi.org/10.1016/J.SCITOTENV.2008.11.022.
- (10)Thammawong, C.; Opaprakasit, P.; Tangboriboonrat, P.: Sreearunothai, P. Prussian Blue-Coated Magnetic Nanoparticles for Removal of Cesium from Contaminated Environment. Journal of 15 1-10.Nanoparticle Research 2013. (6),https://doi.org/10.1007/S11051-013-1689-Z/TABLES/1
- (11) Anjum, S.; Naseer, F.; Ahmad, T.; Jahan, F.; Qadir, H.; Gul, R.; Kousar, K.; Sarwar, A.; Shabbir, A. Enhancing Therapeutic Efficacy: Sustained Delivery of 5-Fluorouracil (5-FU) via Thiolated Chitosan Nanoparticles Targeting CD44 in Triple-Negative Breast Cancer. *Sci Rep* **2024**, *14* (1), 1–18. https://doi.org/10.1038/S41598-024-55900-1
- (12) Karki, S.; Kim, H.; Na, S. J.; Shin, D.; Jo, K.; Lee, J. Thin Films as an Emerging Platform for Drug Delivery. *Asian J Pharm Sci* **2016**, *11* (5), 559–574. https://doi.org/10.1016/J.AJPS.2016.05.004.
- (13) Long, G.; Sadowski, T.; Guler, M. O.; Benelmekki, M.; Kim, J.-H. Stimulus-Responsive Ultrathin Films for Bioapplications: A Concise Review. *Molecules 2023, Vol. 28, Page 1020* **2023**, *28* (3), 1020. https://doi.org/10.3390/MOLECULES28031020.
- (14) Tran, T. T. D.; Tran, P. H. L. Controlled Release Film Forming Systems in Drug Delivery: The Potential for Efficient Drug Delivery. *Pharmaceutics* 2019, Vol. 11, Page 290 2019, 11 (6), 290. https://doi.org/10.3390/PHARMACEUTICS11060290.
- (15) Bao, Z.; Liu, X.; Liu, Y.; Liu, H.; Zhao, K. Near-Infrared Light-Responsive Inorganic Nanomaterials for Photothermal Therapy. *Asian J Pharm Sci* **2016**, *11* (3), 349–364. https://doi.org/10.1016/J.AJPS.2015.11.123.
- (16) Zhou, Z.; Sun, Y.; Shen, J.; Wei, J.; Yu, C.; Kong, B.; Liu, W.; Yang, H.; Yang, S.; Wang, W. Iron/Iron Oxide Core/Shell Nanoparticles for Magnetic Targeting MRI and near-Infrared Photothermal Therapy. *Biomaterials* 2014, 35 (26), 7470–7478. https://doi.org/10.1016/J.BIOMATERIALS.2014.04.063.

- (17) Gao, W.; Wang, Y.; Zheng, Y.; Cai, X. Prussian Blue Nanoparticle: From a Photothermal Conversion Agent and a Drug Delivery System, to a Bioactive Drug. *Acc Mater Res* **2024**, *5* (6), 687–698. https://doi.org/10.1021/ACCOUNTSMR.3C00260.
- C.; (18)Thammawong, Opaprakasit, P.; Tangboriboonrat, P.; Sreearunothai, P. Prussian Blue-Coated Magnetic Nanoparticles for Removal of Cesium from Contaminated Environment. Journal of Nanoparticle Research 2013. 15 1-10.(6).https://doi.org/10.1007/S11051-013-1689-Z/TABLES/1.
- (19) Cameron, D. A.; Gabra, H.; Leonard, R. C. F. Continuous 5-Fluorouracil in the Treatment of Breast Cancer. *Br J Cancer* **1994**, *70* (1), 120–124. https://doi.org/10.1038/BJC.1994.259
- (20) Abu-Thabit, N. Y.; Hamdy, A. S. Stimuli-Responsive Polyelectrolyte Multilayers for Fabrication of Self-Healing Coatings A Review. *Surf Coat Technol* **2016**, *303* (Part B), 406–424. https://doi.org/10.1016/J.SURFCOAT.2015.11.020.
- (21) Chen, C.; Yao, W.; Sun, W.; Guo, T.; Lv, H.; Wang, X.; Ying, H.; Wang, Y.; Wang, P. A Self-Targeting and Controllable Drug Delivery System Constituting Mesoporous Silica Nanoparticles Fabricated with a Multi-Stimuli Responsive Chitosan-Based Thin Film Layer. *Int J Biol Macromol* **2019**, *122*, 1090–1099. https://doi.org/10.1016/J.IJBIOMAC.2018.09.058.
- (22) Ali, A.; Zafar, H.; Zia, M.; ul Haq, I.; Phull, A. R.; Ali, J. S.; Hussain, A. Synthesis, Characterization, Applications, and Challenges of Iron Oxide Nanoparticles. *Nanotechnol Sci Appl* **2016**, *9*, 49–67. https://doi.org/10.2147/NSA.S99986.
- (23) Gao, X.; Wang, Q.; Cheng, C.; Lin, S.; Lin, T.; Liu, C.; Han, X. The Application of Prussian Blue Nanoparticles in Tumor Diagnosis and Treatment. *Sensors* (*Basel*) **2020**, 20 (23), 1–22. https://doi.org/10.3390/S20236905.
- (24) Zhang, X. Q.; Gong, S. W.; Zhang, Y.; Yang, T.; Wang, C. Y.; Gu, N. Prussian Blue Modified Iron Oxide Magnetic Nanoparticles and Their High Peroxidase-like Activity. *J Mater Chem* 2010, 20 (24), 5110–5116. https://doi.org/10.1039/C0JM00174K.
- (25) Marangoni Júnior, L.; Jamróz, E.; Gonçalves, S. de Á.; da Silva, R. G.; Alves, R. M. V.; Vieira, R. P. Preparation and Characterization of

- Sodium Alginate Films with Propolis Extract and Nano-SiO2. *Food Hydrocolloids for Health* **2022**, 2, 100094. https://doi.org/10.1016/J.FHFH.2022.100094.
- (26) Gul, I.; Yunus, U.; Ajmal, M.; Bhatti, M. H.; Chaudhry, G. E. S. Development of Biodegradable Thin Films for Efficient, Specific and Controlled Delivery of Capecitabine. *Biomedical Materials* **2021**, *16* (5), 055019. https://doi.org/10.1088/1748-605X/AC1C61.
- (27) Zhuang, L.; Zhang, W.; Zhao, Y.; Shen, H.; Lin, H.; Liang, J. Preparation and Characterization of Fe3O4 Particles with Novel Nanosheets Morphology and Magnetochromatic Property by a Modified Solvothermal Method. *Sci Rep* **2015**, *5* (1), 1–6. https://doi.org/10.1038/SREP09320
- (28) Shiba, F.; Mameuda, U.; Tatejima, S.; Okawa, Y. Synthesis of Uniform Prussian Blue Nanoparticles by a Polyol Process Using a Polyethylene Glycol Aqueous Solution. *RSC Adv* **2019**, *9* (59), 34589–34594. https://doi.org/10.1039/C9RA07080J.
- (29) Costa, M. J.; Marques, A. M.; Pastrana, L. M.; Teixeira, J. A.; Sillankorva, S. M.; Cerqueira, M. A. Physicochemical Properties of Alginate-Based Films: Effect of Ionic Crosslinking and Mannuronic and Guluronic Acid Ratio. *Food Hydrocoll* **2018**, *81*, 442–448. https://doi.org/10.1016/J.FOODHYD.2018.03.014.
- (30) Passeri, D.; Rossi, M.; Tamburri, E.; Terranova, M. L. Mechanical Characterization of Polymeric Thin Films by Atomic Force Microscopy Based Techniques. *Analytical and Bioanalytical Chemistry* 2012 405:5 **2012**, 405 (5), 1463–1478. https://doi.org/10.1007/S00216-012-6419-3.
- (31) Entezar-Almahdi, E.; Mohammadi-Samani, S.; Tayebi, L.; Farjadian, F. Recent Advances in Designing 5-Fluorouracil Delivery Systems: A Stepping Stone in the Safe Treatment of Colorectal Cancer
 P>. Int J Nanomedicine 2020, 15, 5445–5458. https://doi.org/10.2147/IJN.S257700.
- (32) Joshi, B.; Joshi, A. Polymeric Magnetic Nanoparticles: A Multitargeting Approach for Brain Tumour Therapy and Imaging. *Drug Deliv Transl Res* **2022**, *12* (7), 1588–1604. https://doi.org/10.1007/S13346-021-01063-9/FIGURES/5.